

1 **Experimental Evaluation and Numerical Modeling of Wide-Flange Steel Columns**
2 **Subjected to Constant and Variable Axial Load Coupled with Lateral Drift Demands**

4 Julien Cravero¹; Ahmed Elkady²; and Dimitrios G. Lignos³, M. ASCE
5

6 **Abstract:** This paper presents results from an experimental evaluation on the pre- and post-
7 buckling behavior of 12 steel wide-flange cantilever columns under axial load and lateral drift
8 demands. The influence of several loading and geometric parameters, including the cross-sectional
9 local web and flange slenderness ratios, applied axial load, and lateral and axial loading history on
10 the performance of these columns is thoroughly examined. The test data indicate that cross-
11 sectional local buckling is highly asymmetric in steel columns under variable axial load. A
12 relatively high compressive axial load can significantly compromise the steel column seismic
13 stability and ductility but this also depends on the imposed lateral loading history. The AISC axial
14 load-bending moment interaction equation provides accurate estimates of a steel column's yield
15 resistance. However, the same equation underestimates by at least 30% the column's peak
16 resistance regardless of the loading scenario. Measurements of column flange deformation, axial
17 shortening, flexural resistance and lateral drift are combined in a single graphical format aiding the
18 process of assessing steel column repairability after earthquakes. The test data suggest that current
19 practice-oriented nonlinear component modeling guidelines (PEER/ATC 2010) may not provide
20 sufficient accuracy in establishing both the monotonic and first-cycle envelope curves of steel
21 columns. It is also showed that high-fidelity continuum finite element models shall consider
22 geometric imperfections of proper magnitude in addition to the steel material inelasticity to
23 properly simulate the inelastic buckling of wide-flange steel columns and generalize the findings
24 of physical tests. Issues arising due to similitude are also discussed to properly limit steel column
25 instability modes in future studies.

¹ PhD candidate, HMCO|Navier, Ecole des Ponts ParisTech, Champs-sur-Marne, France. E-mail: julien.cravero@enpc.fr

² Postdoctoral research scientist, RESSLab, ENAC, Swiss Federal Institute of Technology, Lausanne (EPFL), Lausanne, Switzerland. E-mail: ahmed.elkady@epfl.ch

³ Associate professor, RESSLab, ENAC, Swiss Federal Institute of Technology, Lausanne (EPFL), Lausanne, Switzerland. E-mail: dimitrios.lignos@epfl.ch

26 **Keywords:** Steel columns; Large-scale testing; Axial shortening; Axial load carrying capacity;
27 Column repairability curve; Nonlinear modeling of steel columns; ATC 72; Continuum finite
28 element models; Scale effect

29 **Introduction**

30 Steel columns are essential structural components in preventing earthquake-induced collapse
31 of steel frame buildings. For this purpose, capacity design principles are employed to limit inelastic
32 energy dissipation to selected structural fuses, such as steel beams in steel moment-resisting frames
33 (MRFs) or steel braces in concentrically braced frames (CBFs). However, first-story steel MRF
34 columns near their base are still likely to experience inelastic rotation demands due to the
35 deformation kinematics of a full-frame yield mechanism. Albeit capacity-design protection is
36 applied, steel frame buildings may still experience unanticipated column plastic hinging at higher
37 stories due to force redistributions occurring after the onset of component deterioration in strength
38 and stiffness (Lignos et al. 2011b; Lignos et al. 2013; Tirca et al. 2015; Stoakes and Fahnstock
39 2016; Nakashima et al. 2018) or due to higher mode effects (Gupta and Krawinkler 2000; Alavi
40 and Krawinkler 2004; Tremblay 2018).

41 Although columns in prospective steel MRF designs typically experience modest axial load
42 demands of up to 30% of their axial yield strength, P_y , (NIST 2010a; Elkady and Lignos 2014;
43 Suzuki and Lignos 2014; Elkady and Lignos 2015b), columns in existing steel MRF tall buildings
44 may experience axial load demands on the order of 50%~70% P_y (Bech et al. 2015; Akcelyan and
45 Lignos 2018). From a retrofit perspective, it may be challenging to retain a cost efficiency because
46 the ASCE 41 standard (ASCE 2014) would treat these columns as forced-controlled elements (i.e.,
47 zero plastic deformation capacity), regardless of their respective local cross-sectional and member
48 slenderness geometric properties. This assumption was mostly justified based on research
49 conducted in the early 1970s on small-scale column specimens (Popov et al. 1975). However,
50 recent work (Newell and Uang 2006; Elkady and Lignos 2016; Ozkula et al. 2017; Elkady and
51 Lignos 2018a, b) suggests that the same assumption may not be justifiable for “stocky” wide-
52 flange columns with web slenderness ratios $h/t_w < 20$ and member slenderness ratios $L_b/r_y \leq 80$ (L_b
53 is the column’s unbraced length; r_y is the cross-section’s radius of gyration with respect to its
54 weak-axis). However, available experimental data on steel columns subjected to high compressive
55 axial load demands ($\geq 0.5P_y$) coupled with lateral drift demands is still scarce to further
56 substantiate a potential change of the corresponding limit for force-controlled elements as well as
57 the current ANSI/AISC 360-16 (AISC 2016) axial compressive limit of $0.75P_y$ for the plastic
58 design of steel columns with plastic hinges. This data could be potentially useful for the seismic

59 design of steel CBF columns. Although these are primarily subjected to high axial load demands,
60 the column flexural demands could considerably increase due to the non-uniform inelastic drift
61 demands along the steel CBF height (Toutant et al. 2017).

62 From a repairability stand point, FEMA P58 (FEMA 2009a) provides recommendations for
63 typical repair measures and their cost estimates for damage states associated with flexural yielding,
64 cross-sectional local buckling and weld fracture in the aftermath of earthquakes. However, these
65 are mostly applicable to steel beams in fully restrained beam-to-column connections. Although
66 some of these measures (e.g. heat straightening) may be applicable to steel columns, these repairs
67 could become challenging due to potential residual axial shortening (MacRae et al. 1990; Ozkula
68 et al. 2017; Elkady et al. 2018; Elkady and Lignos 2018a). One should also factor that depending
69 on the cross-sectional slenderness, the reserve capacity of a steel column after a seismic event may
70 not necessary be much depending on the imposed lateral drift demands.

71 From a nonlinear modeling stand point, current guidelines for performance-based seismic
72 design and assessment (LATBSDC 2017; PEER 2017) of new and existing steel buildings
73 necessitates the use of component hysteresis models of varying complexities to properly trace the
74 onset of geometric instabilities (e.g. local buckling and lateral torsional buckling) that could
75 significantly compromise the structural behavior at ultimate limit states. This is also an apparent
76 necessity to properly characterize the collapse risk of prospective designs that consider new lateral
77 load resisting systems based on formally established collapse risk-assessment methodologies
78 (FEMA 2009b). Current guidelines (PEER/ATC 2010) facilitating the above needs, mainly cover
79 modeling recommendations for concentrated plasticity phenomenological deterioration models
80 (e.g., Ibarra et al. 2005) due to their computational efficiency. These recommendations were
81 primarily benchmarked to experimental data from fully restrained beam-to-column connections
82 that became available after the 1994 Northridge earthquake (FEMA 2000; Lignos and Krawinkler
83 2011, 2013). Therefore, their applicability to the nonlinear modeling of steel columns shall be
84 carefully examined since PEER/ATC (2010) modeling guidelines neglect important loading (e.g.,
85 axial load) and geometric parameters (e.g., L_b/r_y) that may significantly affect the column behavior
86 under cyclic loading. The need for more monotonic test data in addition to the ones based on
87 reversed cyclic loading is also apparent (Haselton et al. 2008; Krawinkler 2009). The reason is that
88 a monotonic backbone curve, which is considered as a unique property of a structural component,
89 is typically used to benchmark models that explicitly capture component cyclic deterioration in

strength and stiffness for use in nonlinear dynamic analysis (Lignos and Krawinkler 2011; Hamburger et al. 2018).

Furthermore, with computational advancements and the use of high-performance computing, high fidelity continuum finite element (CFE) models are used more and more in explicit collapse simulations of steel frame buildings (Miyamura et al. 2015; Wu et al. 2018a). Despite of the associated computational cost, challenges in this case arise on how to reliably trace the onset and progression of geometric instabilities, as well as the potential coupling of different instability modes, in an explicit manner such that cyclic deterioration in flexural and axial strength of the column can be reliably predicted. Several modeling proposals are available regarding the above matters (Newell and Uang 2006; Elkady and Lignos 2015a; Araújo et al. 2017; Elkady and Lignos 2018b; Wu et al. 2018b) with conflicting recommendations. In that respect, column physical experiments are also needed to benchmark various modelling options and provide coherent recommendations for high fidelity CFE modeling. These models could significantly expand the range of available steel column data by considering a broader range of parameters and configurations that may not be feasible to be physically tested. As such, experiments and complementary CFE simulations can address future challenges regarding the seismic design of steel structures (Uang and Bruneau 2018).

With the goal of further comprehending the hysteretic behavior of wide-flange steel columns to address most of the above challenging issues, this paper summarizes the findings from an experimental program involving 12 large-scale wide flange steel columns tested in a cantilever fashion. The specimens are approximately two-thirds of full-scale as compared to columns used in typical steel frame buildings designed in seismic regions. The loading schemes comprise monotonic and reversed cyclic lateral drifts coupled with relatively high constant and variable axial load demands. The tests reported herein are part of a broader research study that examines the seismic stability of steel columns due to local and member instabilities, considering the development and validation of component modeling techniques of various fidelities for the seismic assessment of steel members and structures.

Description of the Test Program

Table 1 summarizes the test matrix parameters. Three cross-sections are utilized: W14x61 (Group A), W14x82 (Group B) and W16x89 (Group C). Each group includes four nominally

120 identical specimens. These sizes are representative of first-story columns in mid-rise MRFs (4 to
121 8 stories) at a two-third scale. The W14x82 and W16x89 cross-sections satisfy the ANSI/AISC
122 341-16 ([AISC 2016a](#)) compactness limits for highly ductile members, λ_{hd} , regardless of the applied
123 compressive axial load ratio, P/P_y (P is the applied axial load; P_y is based on the measured
124 geometric and material properties of a specimen). These two cross-sections have similar flange
125 slenderness ratios ($b_f/2t_f = 5.9$) but different web slenderness ratios. The W14x61 cross-section has
126 a flange slenderness ratio ($b_f/2t_f = 7.8$) slightly higher than the ANSI/AISC 341-16 flange
127 compactness limit for highly ductile members ($\lambda_{hd} = 7.2$).

128 The test specimens, which were manufactured from three different steel heats, are fabricated
129 from [ASTM \(2015\)](#) A992 Grade 50 steel (nominal yield stress, $f_{yN} = 345\text{ MPa}$). The material
130 properties based on the mill certificate are summarized in [Table 1](#). The same table reports the
131 measured steel material properties based on uniaxial tensile coupon testing ([ASTM 2014](#)). The
132 reported values are the average ones from three coupons extracted from a cross-section's web and
133 flanges. In brief, the steel materials in Groups A, B, and C have a measured yield stress, f_y , that is
134 6%, 9%, and 16% larger than the nominal one, respectively. These values are consistent with the
135 expected-to-nominal yield stress ratio, R_y , of 1.1 for ASTM A992 Grade 50 steel ([AISC 2016a](#)).

136 [Figure 1](#) shows the overall test setup used for the experimental testing of cantilever steel column
137 specimens. The setup comprises a 12MN high capacity vertical actuator and a 1MN horizontal
138 actuator with a $\pm 250\text{mm}$ stroke. In-plane bracing is employed as shown in [Fig. 1](#) to provide in-
139 plane lateral stability to the 12MN vertical actuator. Both actuators are connected, through axially
140 rigid links, to a high precision structural pin at the column specimen's top end. This pin represents
141 a column's inflection point at mid-height by assuming idealized fixed-end boundary conditions at
142 both column ends. Two running beams (noted as guide beams) provide lateral stability bracing at
143 the column specimen's top end. Referring to [Fig. 2](#), the column specimens have a clear length of
144 1750mm and a base-to-pin length of 2150mm. End plates are welded at both column ends with
145 complete joint penetration (CJP) J-groove welds as shown in [Fig. 2](#). The welds were inspected
146 with ultrasonic testing to ensure that potential defects were below the allowable limits as per [AWS](#)
147 ([2009](#)). The weld access holes are designed as per Section J1.6 of [AISC \(2016b\)](#) to ensure
148 minimum stress concentrations at the current weld location.

149 The test program incorporates three lateral loading protocols. These include: i) a monotonic
150 protocol to obtain the monotonic backbone curve of each column specimen at representative

151 gravity-induced axial load ratios and ii) the standard AISC (2016a) symmetric cyclic protocol
152 (Clark et al. 1997), which is commonly used in the pre-qualification of fully restrained beam-to-
153 column connections. In an effort to reduce the total testing time, the symmetric protocol was
154 slightly modified by reducing the number of elastic cycles at the 0.375%, 0.5% and 0.75% drift
155 amplitudes (see Fig. 3a). Lastly, a collapse-consistent lateral loading protocol (Suzuki and Lignos
156 2014) is also employed to investigate the influence of the lateral loading history (i.e., cumulative
157 damage) on a steel column's hysteretic behavior (see Fig. 3b). This protocol represents the seismic
158 demands in steel MRF columns at large deformations associated with structural collapse (Ibarra
159 and Krawinkler 2005; Lignos et al. 2011a). If after the first loading phase, the steel column flexural
160 resistance has not been reduced by more than 50% of its peak flexural resistance, then this protocol
161 is repeated as shown in Fig. 3b. The lateral drift protocols are coupled with constant compressive
162 axial load ratios of 0.3 and 0.5 (see Table 1). A higher axial load ratio of 0.75 was also used to re-
163 assess the ASCE/SEI 41-13 (ASCE 2014) axial load limit for force-controlled elements. Although
164 this axial load demand largely exceeds that expected in steel MRFs (Elkady and Lignos 2014;
165 Suzuki and Lignos 2014), it could be representative in steel CBF columns (Toutant et al. 2017).
166 The symmetric cyclic lateral loading protocol is synchronized with variable axial load demands
167 representing the loading conditions of steel MRF end columns due to dynamic overturning effects
168 (i.e., transient axial load component). The first axial load protocol has a gravity offset, P_g , of 0.30
169 P_y and a transient component, P_v , of $\pm 0.45 P_y$ (i.e., reaching 0.15 P_y in tension and 0.75 P_y in
170 compression as shown in Fig. 3c). The second one involves a gravity load offset of 0.50 P_y and a
171 transient component of $\pm 0.25 P_y$ (see Fig. 3d). The imposed axial loading protocols are fairly
172 conservative because after the onset of column geometric instabilities, the axial load demands are
173 typically relaxed due to force redistributions (Suzuki and Lignos 2014).

174 **Instrumentation and Deduced Column Response Parameters**

175 A total of 27 uniaxial strain gauges are installed on each specimen's web and flanges near their
176 column base over a length of $1.6 d$ (d is the column depth) to track the onset of flexural yielding
177 and plastic strain progression. String potentiometers are used to monitor the in-plane lateral
178 displacement as well as the axial shortening (Δ_{axial}) of a column's top end. Linear variable
179 differential transformers (LVDTs) and inclinometers, installed on a specimen's bottom base plate
180 confirmed the assumption of the fixed end boundary since there was no indication of base plate

181 slip and uplift during the tests. Light-emitting diode (LED) targets are used to track the out-of-
182 plane displacements (δ_{op}) along the column height as shown in Fig. 4. These are also used to track
183 the in-plane displacement of the flange tips (δ_f), which is later on used to assess the feasibility of
184 column repair following earthquakes.

185 Fig. 5 shows the deduced end moment versus the column's chord rotation for all the specimens.
186 Similarly, Fig. 6 shows their axial shortening history versus the chord rotation. Referring to Fig.
187 5, the end moment, M , is measured at the top surface of the column base and is normalized with
188 respect to the plastic bending resistance, M_p of the corresponding cross-section. The M_p is based
189 on the measured geometric and material properties of the respective test specimen. Figure 7 shows
190 the out-of-plane column displacement, δ_{OP} , and the in-plane flange tip displacement, δ_f , histories
191 versus the chord rotation for selected column specimens as defined in Fig. 4. In Figs 5, 6 and 7
192 and the subsequent discussion, the chord rotation, θ , is defined as the in-plane lateral displacement
193 at the column top over its full length, L . In the subsequent sections, a qualitative and quantitative
194 assessment of the steel damage progression is presented including critical aspects associated with
195 the steel column stability under monotonic and cyclic loading.

196 Qualitative Summary of Column Behavior

197 The typical damage sequence of a wide-flange steel column often leading up to the complete
198 loss of its axial-load carrying capacity is illustrated in Fig. 8. During small elastic cycles there is
199 no evident deformation in a test specimen. Referring to Fig. 8a, flexural yielding in the column
200 web and flanges typically occurs at chord rotations ranging from 0.25% to 0.65% radians,
201 depending on the cross-section and the imposed axial load demand. This is visually observed
202 through peeling of the mill-scale at the column surface. Shear yielding is also evident in the web
203 (see Fig. 8a). Upon further lateral loading, the column's fixed end experiences local buckling. The
204 peak of the corresponding local buckling wave is observed at a distance of 0.4 to 0.8 d measured
205 from the column base, as seen in Fig. 8b. The local buckling mode(s) and corresponding
206 amplitudes are mainly dependent on the imposed lateral drift history. In particular, specimens
207 subjected to monotonic and collapse-consistent lateral loading histories experience asymmetric
208 local buckling (Fig. 8b). Drifting in one loading direction (Ibarra and Krawinkler 2005) dominates
209 the column response, thereby leading to asymmetric local buckling. On the other hand, columns
210 subjected to a symmetric cyclic lateral loading history coupled with a constant compressive axial

211 load experience symmetric local buckling as indicated in Fig. 8c. This damage pattern is consistent
212 even in cases that the axial load varies but always remains compressive. Asymmetric local
213 buckling occurs if the axial load demand fluctuates from compression to tension. The reason why
214 the local buckling shape becomes asymmetric in this case is due to neutral-axis shifting that tends
215 to straighten the buckling wave in one of the two loading directions (see Fig. 8e). At larger drift
216 excursions ($\geq 3\%$) a second buckling wave often develops at a distance of 0.8 to 1.6 d ; hence, a
217 full sinusoidal buckling wave is noticeable (see Figs. 8d and 8e). This second buckling wave is
218 accompanied with large out-of-plane displacements near the column's dissipative zone as shown
219 in Fig. 8f. At a lateral drift of 3%, the out-of-plane displacements of the column plastic hinge
220 reaches about 20mm (1.0% L). at this point, the in-plane flange tip displacement is on the order of
221 40mm (see Fig. 7). The magnitude of these displacements affects the repair actions in steel
222 columns in the aftermath of earthquakes as well as the column's reserve capacity that could be of
223 interest in mainshock-aftershock series. The above issues are carefully examined in a subsequent
224 section. Referring to Fig. 8f, the observed out-of-plane instability mode is typically followed by a
225 rapid loss of the column's axial load carrying capacity. This is typically accelerated under a high
226 compressive axial load and/or a high web slenderness ratio. Notably, specimens A4, B3 and C4
227 experienced a sudden loss of their axial load carrying capacity. In particular, in specimen C4
228 (subjected to $0.75 P_y$), axial shortening grew rapidly from 110mm to 170mm (6% to 9% L) within
229 few seconds (see Fig. 6i). Referring to Fig. 5i, this corresponds to a complete loss of the column's
230 flexural resistance.

231 **Quantitative Assessment of Column Behavior**

232 The previous section summarized a number of qualitative features characterizing the behavior
233 of steel columns under lateral drift and axial load demands. This section provides a quantitative
234 assessment of the column hysteretic behavior by considering a number of performance indicators
235 including the cyclic deterioration in a column's flexural resistance, the column axial shortening
236 and the associated plastic hinge length. The influence of the axial load variation on a column's
237 hysteretic response is carefully examined. Issues related to similitude for experimental testing of
238 steel columns are also investigated by means of comparisons with experimental data from prior
239 column testing programs. Finally, based on a synthesis of experimental results, the concept of a

240 column's repairability curve is introduced that may facilitate decision-making for steel column
241 repairs in the aftermath of earthquakes.

242 Column Flexural Resistance

243 [Figure 5](#) shows the moment-rotation relation of the tested specimens. Steel columns experience
244 flexural strength deterioration primarily due to local buckling-induced softening regardless of the
245 employed loading conditions and cross-sectional geometric properties. This is attributed to the
246 relatively small member slenderness ratios ($L_b/r_y < 30$) in all cases. Only in few cases, plastic
247 lateral torsional buckling is coupled with local buckling but only at large drift demands. For
248 instance, for specimen B2 (W16x89, $P/P_y=0.5$), this only occurred after 8% radians under
249 monotonic loading resulting into a steeper negative stiffness in the post-peak response (see [Fig.](#)
250 [5d](#)).

251 Under monotonic lateral loading (see [Figs. 5a, 5d, 5g](#)), the tendency for local buckling initiation
252 decreases with decreasing local web and/or flange slenderness ratios, resulting in increased pre-
253 peak plastic rotation capacities, θ_p (difference between chord rotation at the peak response minus
254 the corresponding column yield rotation). This effect is somewhat pronounced with decreased
255 compressive axial load ratio because a larger portion of the web cross-section experiences tensile
256 stresses at a given lateral drift demand, thereby providing restraint against web local buckling.
257 [Figures 5a and 5b](#) suggest that when local buckling is the primary instability mode of wide-flange
258 steel columns (e.g., Specimens A1, A2 and B1), they attain a residual plateau due to local buckling
259 length stabilization ([Krawinkler et al. 1983](#)). On the other hand, column specimens experiencing
260 coupled local and lateral torsional buckling under monotonic loading (e.g., Specimen B2) attain a
261 second steeper negative stiffness soon after the onset and progression of local buckling. Although
262 inconclusive, this implies that wide flange beam-columns experiencing coupled geometric
263 instabilities under monotonic loading do not necessarily reach to a residual flexural resistance
264 because a buckling length stabilization path cannot be attained. [Figures 5g and 5d](#) indicate that
265 although the local and member slenderness ratios of W16x89 and W14x82 columns are nearly the
266 same (see [Table 1](#)), the former has a θ_p of about 4% while the latter has a θ_p of more than 7% at a
267 given compressive axial load demand. This implies that the respective steel material has a strong
268 influence on the steel column plastic deformation. Albeit all columns are fabricated from
269 nominally identical A992 Gr. 50 steel, the chemical composition of Group C include a notably

270 larger percentage of Manganese than that of Groups A and B. This strongly influences the steel
271 material hardenability (Shirasawa et al. 1981; Bruneau et al. 2011) and in turn the plastic
272 deformation capacity of a steel member prior to the formation of local buckling. In particular,
273 specimens C1 and C2 hardened monotonically much more than specimens A1, A2, B1 and B2 as
274 shown in Figs 5g, 5a and 5d, respectively.

275 Referring to Fig. 5, the hysteretic behavior of wide-flange steel columns under cyclic lateral
276 loading is primarily governed by local buckling in their post-peak response. Columns that are
277 subjected to a constant compressive axial load ratio ($P/P_y \geq 0.5$), experience accelerated cyclic
278 deterioration in their flexural resistance after the onset of local buckling. This is consistent with
279 prior experimental observations (Ozkula et al. 2017; Elkady and Lignos 2018a). Although most
280 columns maintained their flexural resistance at a lateral drift of 2%, the ones subjected to a
281 symmetric cyclic lateral loading history lost their axial load carrying capacity at a lateral drift of
282 4% regardless of their local slenderness ratios. This is mostly attributed to the relatively large
283 number of inelastic drift cycles of a symmetric cyclic lateral loading history. Notably, a W14x61
284 column (Specimen A3), which is moderately compact as per ANSI/AISC 341-16, maintained close
285 to 80% of its flexural resistance up to a lateral drift demand of 6% when subjected to a collapse-
286 consistent lateral loading protocol (see Fig. 5b). This indicates the strong influence of the imposed
287 lateral loading history on the steel column hysteretic response.

288 Column specimens subjected to variable axial load demands developed a fully asymmetric
289 hysteretic behavior (see Figs. 5c and 5f). In particular, while the compressive axial load increases
290 in an absolute sense due to the transient axial load demand in addition to the gravity-induced one,
291 the flexural negative stiffness in a column's post-peak response becomes relatively steep. On the
292 other hand, while a column experiences reduced compressive axial load demand in the opposite
293 lateral loading direction, its flexural resistance does not practically deteriorate. This is attributed
294 to local buckling straightening. Notably, the measured data corresponding to Figs. 5c and 5f should
295 be interpreted as lower bounds of a column's behavior under variable axial load demands. The
296 reason is that the imposed axial load demands are relaxed due to force redistributions occurring
297 within a steel frame building experiencing structural damage. This relaxation may reach up to 50%
298 of the initial axial load demand (Suzuki and Lignos 2014, 2015b).

299 **Assessment of Axial Force – Bending Interaction Curves**

300 The experimental data set covers a wide range of axial load demands, offering the opportunity
301 to evaluate the existing axial force-bending (P-M) interaction curves of current code provisions.
302 [Figure 9](#) shows the ANSI/AISC 360-16 ([AISC 2016](#)) P-M interaction curve. The vertical and
303 horizontal axes are normalized with respect to the available axial and flexural strengths, P_c and M_c ,
304 respectively, according to [AISC \(2016b\)](#). Shown in the same figure are all the measured P-M data
305 points when first yield occurred ([Fig. 9a](#)) and at the maximum attained moment ([Fig. 9b](#)). Referring
306 to [Fig. 9a](#), the P-M interaction curve adequately predicts the flexural resistance at first yield in
307 almost all cases that the axial load demand is constant. The P-M interaction curve under predicts
308 the first yield moment of specimens A4 and B4 by more than 30%. This is because the P-M
309 interaction curve does not depict the influence of axial load variation on the flexural resistance of
310 these columns. Finally, specimen C4 (W14x82, $P/P_y=0.75$) also developed a higher flexural
311 resistance than what is predicted by the P-M interaction curve. However, if the full length member
312 was considered, then member (flexural) buckling could have been the primary instability mode in
313 this case considering the high compressive axial load demand imposed on this column.

314 Vis-à-vis the above discussion, the P-M interaction curve according to the ANSI/AISC 360-16
315 provisions seems rational for predicting a beam-column's flexural resistance at first yield.
316 However, this is not the case for the column's maximum attained moment (see [Fig. 9b](#)) regardless
317 of the imposed compressive axial load demand. In particular, the P-M interaction curves were
318 derived analytically considering beam-columns without acknowledging any hardening (i.e., elastic
319 perfectly-plastic material assumption) ([ASCE 1971](#); [Bruneau et al. 2011](#)). [Figure 9b](#) underscores
320 the influence of the kinematic and isotropic hardening on M_{max} . This is more evident in columns
321 with more compact cross-sections (Groups B and C), in which M_{max} is underestimated by at least
322 30% and 40%, respectively. The delay in the local buckling formation leads to an appreciable
323 amount of cyclic hardening. This is not so apparent in steel columns with moderately ductile cross-
324 sections (i.e., Group A) due to the early onset of geometric instabilities after flexural yielding. The
325 above observations agree with monotonic tests on small-scale specimens with slender cross-
326 sections ($h/t_w=82\sim107$, $b/t_f=5.9\sim6.7$) conducted by [Nakashima et al. \(1990\)](#). The general
327 consensus is that a thorough re-assessment of the P-M interaction curves for steel beam-columns
328 used in seismic applications shall be conducted, which agrees with recent related work ([Zeimian](#)
329 [et al. 2018](#)). Such an assessment is outside the scope of the present paper.

330 **Column Axial Shortening**

331 [Figure 6](#) shows the column axial shortening versus the corresponding column chord rotation.
332 Previous studies ([MacRae et al. 1990; Elkady and Lignos 2018a, b](#)) found that axial shortening is
333 strongly correlated with a steel column's cumulative inelastic rotation demands. Thus, specimens
334 subjected to monotonic lateral loading (see [Figs. 6a, 6d, 6g](#)) exhibit only minor axial shortening
335 of up to 30mm (i.e., 1.4% L) regardless of the cross-section web slenderness ratio and the imposed
336 compressive axial load. In contrast, specimens subjected to symmetric cyclic lateral loading
337 shorten by up to 110mm (6% L) due to the large number of inelastic drift cycles. The higher the
338 web slenderness ratio the larger the column axial shortening because the column web becomes
339 more susceptible to local buckling-induced softening.

340 Although specimen C4 was subjected to a $P/P_y=0.75$, it shortened more-or-less by the same
341 amount with specimen C3 that was subjected to $P/P_y=0.5$ (see [Fig. 6i](#) versus [Fig. 6h](#)). This implies
342 that the neutral-axis position of the cross-section strongly influences the corresponding column
343 axial shortening. In particular, in the above two cases, due to the high compressive axial load, the
344 neutral axis always remained outside the cross-section. As such, the cross-section's entire web
345 experienced compressive stresses throughout the imposed lateral drift history. [MacRae et al.](#)
346 ([2009](#)) found that the column axial shortening is practically not influenced by the applied
347 compressive axial load if $P/P_y > A_w/A$ (in which, A_w and A are the web area and gross cross-section
348 area, respectively). The experimental results suggest that this mechanistic assumption holds true
349 for end steel MRF columns experiencing transient axial load demands if the imposed axial load
350 ratio is still above the threshold value of A_w/A despite of the corresponding axial load variation
351 range. In particular, referring to [Figs. 6e](#) and [6f](#), Specimens B3 ($P/P_y=0.5$) and B4
352 ($P_g/P_y=0.5 \pm P_v/P_y=0.25$) are subjected to the same lateral drift histories but considerably different
353 axial load demands. Nonetheless, they both experienced nearly the same axial shortening due to
354 the aforementioned reason.

355 **Effect of Transient Axial Load**

356 [Figure 10](#) shows the history of axial load ratio variation versus the column axial shortening,
357 Δ_{axial} , for two specimens (A4 and B4). In order to quantify their axial stiffness deterioration, the
358 instantaneous stiffnesses, K_{axial}^- and K_{axial}^+ , corresponding to the beginning and the end of each
359 lateral drift loading excursion, respectively, are extracted as illustrated in [Figs. 10a](#) and [10b](#). The
360 $K_{axial}^{+/-}$ values are normalized with respect to the elastic axial stiffness, $K_{axial,el}$, of the respective

361 column based on measured geometric and material properties (i.e., $K_{axial,el}=EA/L$). Accordingly,
362 the normalized axial stiffness, K_{axial} is shown [Figs. 10c-d](#), for the first excursion of each drift level
363 of the employed lateral loading protocol. In both cases, the axial stiffness deteriorates rapidly right
364 after the onset of web and flange local buckling of column specimens A4 and B4. This is more
365 evident in the negative loading direction when the compressive axial load reaches 75% P_y
366 ($K_{axial}^+/K_{axial,el}=54\%$ and 34% for specimen A4 and B4, respectively). While the lateral drift
367 progresses, the rate of axial stiffness degradation stabilizes until the axial load carrying capacity is
368 lost ($K_{axial}^+=0$). This limit state is depicted relatively well in [Fig. 10a](#) for Specimen A4. On the
369 other hand, Specimen B4 lost its axial load carrying capacity during the last lateral loading
370 excursion as shown in [Fig. 10b](#). To the best of the authors knowledge, the data presented herein is
371 unique and can facilitate the calibration of mechanics-based numerical models that explicitly
372 capture axial stiffness degradation as well as column axial shortening ([Suzuki and Lignos 2017](#);
373 [Do and Filippou 2018](#); [Kolwankar et al. 2018](#)).

374 Plastic Hinge Length

375 [Figure 11a](#) shows the measured plastic hinge length, L_{PH} , (defined as the length between the
376 column base plate and the last cross-sectional level experiencing plastic strains) for all the column
377 specimens. From this figure, the W14x61 and W16x89 specimens developed an L_{PH} of 1.6~2.0 d .
378 The stockier W14x82 specimens developed a fairly large L_{PH} of 2.0~2.6 d . The spread of yielding
379 at the column base relates to the steel material hardening ([Kanno 2016](#)) and the corresponding
380 cross-section local slenderness ratio. In particular, if the onset of local buckling is delayed, then
381 the spread of plasticity becomes large for mild steels exhibiting combined kinematic/isotropic
382 hardening. This is the reason for the notable differences between the measured plastic hinge length
383 between specimens in Group C and Groups A and B. While all three steel heats were nominally
384 the same (i.e., A992 Gr. 50), the chemical composition of the Group C steel material includes a
385 notably larger percentage of Manganese. As stated earlier, this influences the steel material
386 hardenability ([Shirasawa et al. 1981](#); [Bruneau et al. 2011](#)) and in turn the extent of plastic hinge
387 length of a steel member.

388 [Figure 11a](#) suggests that the employed lateral loading protocol has a negligible effect on the
389 column plastic hinge length (e.g. specimen B2 versus B3 and similarly C2 versus C3). On the other
390 hand, the presence of high compressive axial load demands augments the plastic hinge length. The

resultant second-order moment due to the compressive axial load pushes the center of local buckling further away from the column base, thereby increasing the associated plastic hinge length. This is schematically illustrated in Fig. 11b. In particular, specimens A2 and B2 ($P/P_y=0.5$) developed a 12% larger plastic hinge length compared to specimens A1 and B1 ($P/P_y=0.3$), respectively. Similarly, specimen C2 developed a plastic hinge length that is 30% larger than specimen C1. The above observations reflect the findings from prior related experimental studies (Nakashima et al. 1990; Peng et al. 2008; Suzuki and Lignos 2015a; Elkady and Lignos 2016).

Also superimposed in Fig. 11a is the predicted L_{PH} values based on the Elkady and Lignos (2018b) empirical model. This model was developed based on high-fidelity CFE simulations of steel columns under cyclic loading. In particular, the proposed empirical model relates L_{PH} to the web slenderness ratio, h/t_w , the member slenderness ratio, L_b/r_y , and the compressive axial load ratio, P/P_y . Although the empirical model predicts relatively well the plastic hinge length of Group A and B specimens, it underestimates L_{PH} by 40%, on average, for the Group C specimens. This is primarily related to the associated variability in material-hardening properties that is not captured by this empirical model. Notably, the observed plastic hinge lengths of Groups A and B are in a reasonable agreement with the minimum L_{ph} of 1.5 d specified in the New Zealand standards, NZS 3404 (SNZ 2007), for Category 1 and 2 members (equivalent to highly ductile members per ANSI/AISC 341-16).

Vis-à-vis the above discussion, the experimental results facilitate the identification of the potential plastic hinge length of a steel column for member stability verifications.

Section Classification and Scale Effects

In general, deep wide-flange steel columns ($d > 400\text{mm}$) are prone to geometric instabilities associated with local and/or lateral torsional buckling (NIST 2010b). In a recent testing program (Elkady and Lignos 2018a), the second and third authors tested a 4m long fixed-end column with a deep W24x146 cross-section under symmetric cyclic loading combined with a constant $P/P_y=0.5$. This specimen had a comparable web and flange local slenderness ratio with specimen C3 (W16x89) tested herein. The pre-dominant instability mode in both specimens was local buckling-induced softening followed by column axial shortening (Elkady and Lignos 2018a) as indicated in Figs. 12a and 12b. Due to the apparent similarity of the two specimens in their loading and base boundary conditions as well as their local cross-sectional slenderness ratios, the “deep-column”

421 effect on the steel column stability can be properly characterized. Issues related to similitude for
422 future experimental studies related to the seismic stability and ductility of steel columns can be
423 highlighted. In particular, Fig. 12c shows a comparison of the normalized moment-rotation
424 relations of the two specimens. Although both specimens reached to a comparable normalized
425 peak moment, the W24x146 column experienced local buckling early on in the lateral loading
426 history compared to the W16x89 steel column. This is attributed to the restraint that the flange
427 provides to the web against local buckling. In particular, the web of the W24x146 cross-section is
428 less restrained by the flanges against local buckling compared to the W16x89 cross-section. For
429 the same reason, at any given drift following the onset local buckling, column axial shortening in
430 the W24x146 column was about 2 times larger than that of the W16x89 column as shown in Fig.
431 12d. This simple comparison highlights the need to re-define the cross-sectional compactness
432 limits in future design provisions by acknowledging the interaction between the web and flanges
433 rather than treating those limits as an individual plate rule whereas the section classification limits
434 are determined by comparing the most slender plate between the web and flange with the
435 respective codified slenderness limits (Chen et al. 2013).

436 A side aspect to be thought through carefully is the proper scaling selection to characterize the
437 hysteretic behavior of deep columns. Although informative, prior studies (Zargar et al. 2014)
438 attempting to characterize the behavior of deep columns through relatively small-scale
439 experiments, observed instability modes that departed from those observed at full-scale. Similar
440 issues have been raised in fracture-related problems when fracture toughness is transferred from
441 lab- to real-scale components (Pericoli and Kanvinde 2018).

442 Column Repairability Curves

443 The feasibility of conducting column repairs in the aftermath of earthquakes can be typically
444 decided based on the extent of damage represented by the magnitude and size of the local buckling
445 wave (FEMA 2009a). The experimental program discussed herein as well as prior physical testing
446 of wide-flange steel columns (MacRae et al. 1990; Newell and Uang 2006; Suzuki and Lignos
447 2015b; Ozkula et al. 2017; Elkady and Lignos 2018a) highlight that steel columns may experience
448 significant residual axial shortening. This could compromise the steel column repairability.
449 Moreover, from a structural safety stand point, another compelling issue is the reserve capacity of

450 a steel column after a mainshock. Reconnaissance reports indicate that aftershocks could often be
451 quite damaging leading to structural collapse (Clifton et al. 2011; Okazaki et al. 2013).

452 In this regard, the concept of “Column Repairability Curve” is introduced herein to integrate all
453 the aforementioned damage indicators into a single compact graphical format to facilitate the
454 decision-making for steel column repair actions in the aftermath of earthquakes. Figure 13 shows
455 such curves for different column specimens experiencing both asymmetric (see Figs. 13a, 13b)
456 and symmetric local buckling (see Fig. 13c) near the column base. These curves combine three
457 interdependent column performance indicators with the column lateral drift demand, θ . In
458 particular, these indicators include the normalized residual flexural resistance of a steel column as
459 a function of the peak flexural resistance, M_{max} (top horizontal axis); the corresponding column
460 axial shortening, Δ_{axial} (right vertical axis); and the flange tip displacement, δ_f , indicating the local
461 buckling wave amplitude (left vertical axis). This displacement is extracted from LED
462 measurements shown in Fig. 7. Note that in the column repairability curves, axes are not in scale.

463 Referring to Figs. 13a and 13b, for columns experiencing asymmetric buckling, the
464 corresponding flange tip displacement is almost double the column residual axial shortening. At
465 lateral drift demands of 2% (representative of a design-basis earthquake), column repairability by
466 means of straightening and/or strengthening the buckled region is feasible considering that both δ_f
467 and Δ_{axial} are less than 10mm. Although the corresponding residual flexural resistance of these
468 columns at a 2% drift demand is almost 80% M_{max} , this loss can be restored with the above repair
469 measures. Referring to Fig. 13c, for columns experiencing symmetric local buckling, Δ_{axial} and δ_f
470 are nearly the same. Due to the exponential increase of residual axial shortening, a column may
471 practically be unrepairable after 2% radians. It is acknowledged that the repairability assessment
472 is subject to an expert’s opinion as well as the building characteristics and regional design practices.
473 The column repairability curves presented herein are indicative and can provide a quantitative
474 assessment of a steel column’s damage state if the expected lateral drift demands can be somehow
475 estimated. These curves can also be used as a tool to quickly estimate the lateral drift demands as
476 well as the flexural resistance loss if physical measurements of the flange tip displacement and/or
477 column residual shortening are conducted after an earthquake.

478 **Assessment of Nonlinear Modeling Recommendations for Wide Flange Steel Columns**

479 **PEER/ATC 72-1 Modeling Guidelines**

480 PEER/ATC 72-1 ([PEER/ATC 2010](#)) provides engineering practice-oriented nonlinear
481 modeling guidelines for structural steel components for the nonlinear seismic performance
482 assessment of existing and prospective structural designs. These guidelines employ idealized
483 concentrated plasticity component models for use in nonlinear static and response-history analyses
484 of frame structures. These recommendations are largely based on physical testing of steel beams
485 in fully restrained beam-to-column connections ([FEMA 2000; Lignos and Krawinkler 2011](#)). Due
486 to lack of column test data at the time, it is common that the same recommendations are used for
487 the nonlinear modeling of wide-flange steel columns. In particular, PEER/ATC 72-1 *Option 1*
488 defines the input model parameters for the monotonic backbone curve of a steel structural
489 component. This is treated as a unique property of the structural component and shall be used with
490 hysteretic component models that explicitly simulate cyclic deterioration in strength and stiffness
491 ([Ibarra et al. 2005; Krawinkler 2009; Lignos and Krawinkler 2011](#)). Alternatively, in order to
492 conduct a nonlinear static analysis, PEER/ATC 72-1 *Option 3* modeling option is employed. This
493 represents the first-cycle envelope curve of a structural component subjected to a symmetric cyclic
494 lateral loading protocol. This curve, which is loading history dependent, only captures implicitly
495 the influence of cyclic deterioration on a component's strength and stiffness. The above nonlinear
496 modeling options are evaluated herein based on direct comparisons with the gathered experimental
497 data. To facilitate the subsequent discussion, selected comparisons are established based on tests
498 conducted under monotonic (see [Figs. 14a and 14b](#)) and cyclic lateral loading (see [Figs. 14c, 14d](#)).

499 **Elastic Effective Stiffness, K_e**

500 Referring to [Fig. 14](#), the PEER/ATC 72-1 modeling guidelines tend to overestimate the elastic
501 stiffness, K_e , of wide-flange steel columns because the contribution of the shear deformations is
502 neglected in the K_e computation. In principle, a member's total lateral deformation can be
503 expressed as $\delta_{total} = \delta_b(1+\alpha)$ in which, δ_b is the flexural deformation; and α is the bending-to-shear
504 stiffness ratio ($\alpha = K_b/K_s$). For instance, when the shear stiffness is infinitely large ($K_s=\infty$), α
505 approaches zero implying no shear deformations. For the range of cross-sections summarized in
506 [Table 1](#), α was found to be about 0.25, which corresponds to a 25% increase of a column's elastic
507 deformation. More recently, [Elkady and Lignos \(2018a\)](#) found that this issue is prevalent in deep
508 wide-flange steel columns. [Figure 15](#) summarizes the ratio of the theoretically-computed stiffness
509 to the measured one from 152 wide-flange steel column experiments ([Popov et al. 1975; MacRae](#)

510 et al. 1990; Nakashima et al. 1990; Newell and Uang 2006; Cheng et al. 2013a; Cheng et al. 2013b;
511 Suzuki and Lignos 2015b; Ozkula et al. 2017; Elkady and Lignos 2018a) including the test data
512 presented herein. The figure shows that K_e is overestimated, on average, by 30% when shear
513 deformations are neglected. Accordingly, it is recommended that shear deformations be considered
514 when computing a wide-flange steel column's effective stiffness, K_e . The corresponding formula
515 for estimating the elastic effective stiffness of energy-dissipative links in eccentrically braced
516 frames would suffice for this purpose (Bech et al. 2015; Lignos et al. 2018).

517 **Effective Yield Strength, M_y^* , and Capping Strength, M_{max} ,**

518 The PEER/ATC 72-1 modeling *Options 1* and *3* compute the corresponding effective yield
519 strength as $M_y^* = 1.1 Z f_{ye} (1 - P/P_y)$ where, Z is the cross-section plastic modulus about the strong-
520 axis; and f_{ye} is the expected yield stress. The predicted M_y^* tends to underestimate the measured
521 one as demonstrated in Fig. 14. This is attributed to (a) the axial load-bending interaction that is
522 only considered approximately from the equation above; and (b) the corresponding material cyclic
523 hardening that is inherently captured by the coefficient 1.1 (Lignos and Krawinkler 2011). The
524 former can be easily noted from Figs. 14a and 14b representing specimens subjected to $P/P_y =$
525 30% and 50%. The latter is justified from a comparison of the first-cycle envelopes of nominally
526 identical specimens subjected to a symmetric and a collapse-consistent lateral loading history as
527 shown in Figs. 14c and 14d, respectively. In particular, due to the relatively small number of
528 inelastic cycles prior to the onset of local buckling, cyclic hardening is not as pronounced as it is
529 in the case of a symmetric cyclic lateral loading history. As such, the predicted M_y^* is nearly the
530 same with the measured one (see Fig. 14d).

531 The PEER/ATC 72-1 modeling guidelines suggest a constant capping-to-effective-yield
532 strength ratio, M_{max}/M_y^* , of 1.1 that depicts the effects of material hardening on the post-yield
533 behavior of a structural steel component. Albeit this value is fairly constant for steel beams due to
534 the absence of axial load demands (Lignos and Krawinkler 2011), the test data herein indicate that
535 M_{max}/M_y^* varies from 1.1 to 1.7 for Group A and B specimens; and up to 2.4 for Group C specimens.
536 In particular, Group B and C specimens involve cross-sections with fairly compact webs, thereby
537 delaying the onset of local buckling which in turn translates into a relatively high hardening ratio,
538 $M_{max}/M_y = 1.5$. Accordingly, for nonlinear phenomenological component modeling, M_{max}/M_y^* shall

539 be computed by considering the cross-sectional slenderness and the corresponding axial load
540 demand (Lignos et al. 2018).

541 **Pre- and post-peak Plastic Rotations**

542 Figures 16a and 16b summarizes the pre- (θ_p) and post-peak (θ_{pc}) plastic rotations, respectively,
543 of the 12 tested column specimens. These values are deduced based on idealized trilinear curves
544 fitted to the monotonic backbone and first-cycle envelope curves of each column specimen.
545 Superimposed in the same figures are the computed values based on the PEER/ATC 72-1 modeling
546 guidelines (both *Options 1* and *3*). Although the test data highlight the dependence of the achieved
547 plastic rotation capacities on the cross-sectional local slenderness ratios and the applied axial load
548 demand, the predicted values depict the former but not the latter effect. As noted earlier, the
549 PEER/ATC 72-1 *Option 1* equations were developed based on test data from steel beams (i.e., zero
550 axial load). As such, the computed values tend to overestimate the measured ones based on
551 monotonic loading by at least 20%, when $P/P_y > 0.3$ and/or the corresponding cross-sectional web
552 slenderness, $h/t_w > 25$. With regards to column specimens subjected to symmetric cyclic lateral
553 loading, *Option 3* systematically overestimates both θ_p and θ_{pc} values by at least 50%. Noteworthy
554 stating that for Specimen A3, which was subjected to a collapse-consistent lateral loading history,
555 the predicted θ_{pc} value was well correlated with the measured one. This suggests the need for more
556 refined lateral loading protocols for component modeling and acceptance criteria of structural
557 components (Suzuki and Lignos 2014; Maison and Speicher 2016).

558 **Continuum Finite Element Modeling Recommendations for Wide-Flange Steel Columns**

559 High-fidelity CFE models can be effectively utilized to simulate the onset and progression of
560 geometric instabilities associated with local and/or lateral torsional buckling in wide-flange steel
561 columns under monotonic and cyclic loading. A number of recommendations are available for this
562 purpose in the literature (Newell and Uang 2006; Elkady and Lignos 2015a; Fogarty and El-Tawil
563 2015; Araújo et al. 2017; Elkady and Lignos 2018b) with conflicting conclusions. In particular,
564 Elkady and Lignos (2015a, 2018b) and Fogarty and El-Tawil (2015) suggest that local and member
565 geometric imperfections (GIs) are of equal importance to properly simulate the onset of geometric
566 instabilities due to local and lateral torsional buckling along a steel column that utilizes slender
567 cross-sections. Others suggest that GIs are only important for properly simulating the monotonic

568 behavior of steel beam-columns but not the cyclic one (Araújo et al. 2017). A more recent study
569 (Wu et al. 2018a) suggested that GIs shall not be used for modeling the hysteretic behavior of deep
570 and slender steel columns such that pre-selected bifurcation paths can be avoided. In prior studies
571 (Newell and Uang 2006), GIs were neglected but these were not deemed to be critical for
572 simulating the hysteretic behavior of columns utilizing stocky cross-section profiles. This section
573 clarifies several of the aforementioned concepts in an intrinsic effort to provide guidance for CFE
574 nonlinear modeling of steel columns. For this purpose the commercial finite element software
575 **ABAQUS-FEA/CAE (2011)** is utilized with the following assumptions; The large deformation
576 simulations employ quadratic shell elements with reduced integration (S4R) that are deemed to
577 adequately trace geometric instabilities (Elkady and Lignos 2015a, 2018b). Material nonlinearity
578 is considered with the Von Mises yield surface and a multiaxial plasticity model (Voce 1948;
579 Armstrong and Frederick 1966; Lemaître and Chaboche 1975), which was calibrated to uniaxial
580 cyclic coupon tests of (ASTM 2015) A992 Gr. 50 steel (Suzuki and Lignos 2017) of similar
581 microstructure and chemical composition with the steel materials discussed herein. The material
582 model parameters are loading history independent (Elkady and Lignos 2018b; Sousa and Lignos
583 2018). Two types of analyses are conducted with (w) and without (w/o) triggering local and
584 member imperfections (GIs) based on conventional buckling analysis. Local imperfections are set
585 to $b_f/250$ and $h_w/250$ based on imperfection measurements conducted in prior testing programs
586 (Elkady and Lignos 2016; Elkady and Lignos 2018a) for a similar range of cross-section profiles
587 with the ones discussed herein. The above geometric imperfections are within the manufacturing
588 limits of wide-flange products (ASTM 2014).

589 Figure 17 shows sample comparisons between the CFE predictions and the test data of
590 representative specimens to address the above issues. Referring to Figs. 17a and 17b, the
591 agreement between the simulated and measured responses is noteworthy when GIs are considered
592 both for monotonic and cyclic lateral loading. The same figure also shows the simulated results
593 when local GIs are not incorporated in the CFE model. The results suggest that the CFE simulation
594 model in this case overestimates by at least a factor of two the flexural resistance and plastic
595 deformation capacities of steel columns under monotonic and/or cyclic loading. These simple
596 comparisons suggest that CFE simulation models shall (a) properly consider the combined
597 kinematic/isotropic hardening of mild steels and (b) always incorporate GIs of proper magnitude
598 to accurately trace the onset of local and/or lateral torsional buckling of steel wide-flange beam-

599 columns. Recommendations developed by the second and third author ([Elkady and Lignos 2018b](#))
600 can facilitate this effort. These agree with recent modeling recommendations on how to model
601 complex three-dimensional behavior of steel members ([Zeimian et al. 2018](#)).

602 **Summary and conclusions**

603 This paper discusses in detail the main findings from an experimental program that
604 characterized the behavior of wide-flange steel columns under monotonic and reversed cyclic
605 lateral loading coupled with high constant and variable axial load demands. The tests were
606 conducted with 1800mm long cantilever test specimens. Test parameters included the cross-
607 section local slenderness, the applied axial load ratio (constant versus variable) as well as the lateral
608 loading history. The test program also offered the opportunity to assess the state-of-the-art
609 recommendations for models of various computational resolutions including concentrated
610 plasticity and high-fidelity continuum finite element (CFE) approaches.

611 The typical damage progression of the test specimens involved flexural yielding followed by
612 cross-sectional local buckling regardless of the employed loading history. Due to the relatively
613 small member slenderness, L_b/r_y , of the test specimens, global instabilities (i.e., lateral torsional
614 and/or flexural buckling) were not evident at lateral drift amplitudes of up to 7% even at high axial
615 load demands ($P/P_y > 0.5$). The local buckling mode was fairly symmetric in test specimens under
616 symmetric lateral loading histories coupled with constant compressive axial load. On the other
617 hand, wide-flange steel columns subjected to asymmetric lateral loading or variable axial load
618 demands (that varies between compression and tension) developed an asymmetric local buckling
619 mode. The plastic hinge region varies from $1.6 d$ to $2.5 d$ with the center of local buckling moving
620 away from the column base with higher compressive loads. However, this becomes insensitive to
621 the compressive axial load ratio if becomes larger than a threshold equal to web-to-total cross-
622 section area ratio.

623 Under monotonic lateral drift, the test results suggest that steel columns subjected to modest
624 axial load demands ($P/P_y = 0.30$) attain a residual flexural strength due to stabilization of the
625 developed cross-sectional local buckling length. On the other hand, steel columns under high axial
626 load demands ($P/P_y \geq 0.5$) typically attain a secondary negative stiffness at large lateral
627 deformations due to coupling of local and lateral torsional buckling. In any case, the loss of a
628 column's axial load carrying capacity is accompanied by severe axial shortening.

629 Columns subjected to high axial load demands and reversed cyclic lateral loading deteriorate
630 in flexural resistance rapidly after a reference lateral drift of 2%. In fact, most of the tested
631 specimens lost their axial load carrying capacity at a lateral drift of 4%. Nonetheless, the test results
632 underscore the influence of the imposed lateral loading history on the column's plastic deformation
633 capacity. Although inconclusive, seismic acceptance criteria should eventually consider the
634 cumulative plastic rotation demands in addition to a reference plastic deformation.

635 The hysteretic behavior of steel columns under variable axial load demands is highly
636 asymmetric. The increased compressive axial load due to the transient effects causes local buckling
637 initiation at the column flange experiencing the highest compressive stresses. In the opposite
638 loading direction, the flexural resistance of the column is maintained to at least 80% of the
639 maximum attained moment even at lateral drift demands of up to 4% due to local buckling
640 straightening. In this case, the experimental results shall be interpreted as lower bound responses
641 because the imposed variable axial loading histories conservatively ignored the redistribution of
642 axial forces within a steel frame building once its structural members enter into the inelastic regime.
643 This issue deserves much attention in future experimental studies.

644 The ANSI/AISC 360-16 ([AISC 2016b](#)) axial load–bending (P-M) interaction curve predicts
645 relatively well the first flexural yielding of all the test specimens. However, the P-M interaction
646 curve under predicts by at least 30% the peak column flexural resistance regardless of the imposed
647 axial load demand. This is due to the fact that this interaction curve does not acknowledge the post-
648 yield hardening of typical mild steel materials (i.e., assumption of elastic-perfectly plastic material).
649 This assumption seems to work well for steel columns utilizing moderately ductile cross-sections
650 as per ANSI/AISC 341-16 ([AISC 2016a](#)) that develop a negligible amount of cyclic hardening due
651 to the early occurrence of local buckling. At high compressive axial load demands ($P/P_y \geq 0.75$)
652 the P-M interaction shall be carefully evaluated based on prospective tests with column specimens
653 prone to member buckling.

654 The experimental data summarized herein also served for the validation of state-of-the-art
655 component modeling guidelines ([PEER/ATC 2010](#)) widely used by the engineering profession for
656 the seismic performance assessment of existing and prospective steel building designs. In
657 particular, the PEER/ATC 72-1 *Option 1* and 3 component models were thoroughly assessed. The
658 former defines the monotonic backbone curve of a structural component, while the latter defines
659 its first-cycle envelope curve based on experiments conducted with standard symmetric cyclic

660 lateral loading histories. In particular, both *Option 1* and *3* models tend to underestimate a
661 column's elastic lateral stiffness by up to 30% when shear deformations are neglected. The
662 effective flexural strength, M_y^* , is only predicted well for column specimens subjected to modest
663 axial load demands of $0.30P_y$ representative of steel MRF columns. Although the post-yield
664 hardening ratio, M_c/M_y^* , could range anywhere from 1.1 to 1.5 depending on the imposed axial
665 load demand and the cross-sectional web local slenderness, the PEER/ATC 72-1 component
666 models assume a constant value of 1.1, which is typical for steel beams (i.e., zero axial load ratio)
667 with slender but seismically compact cross-sections ([Lignos and Krawinkler 2011](#)). Similarly, the
668 PEER/ATC 72-1 *Option 1* model predicts reasonably well the monotonic backbone curve of wide-
669 flange steel columns under modest axial load demands ($0.30P_y$) and whose web slenderness ratios
670 are within the calibration range of the *Option 1* model ($20 < h/t_w < 55$). In cases that $P/P_y > 0.30$
671 and $h/t_w > 25$, the *Option 1* model over-predicts the corresponding pre- (θ_p) and post-capping (θ_{pc})
672 plastic rotation capacities by at least 20%. Although the ATC/PEER 72-1 *Option 3* model over-
673 predicts the θ_p and θ_{pc} values by at least 50% for steel columns under reversed cyclic lateral loading,
674 much closer predictions are obtained for columns under collapse-consistent lateral loading.

675 Continuum finite element (CFE) models shall always consider geometric imperfections (GIs)
676 to properly trace local buckling of wide-flange steel columns with seismically compact cross-
677 sections near the high ductility limits as per ANSI/AISC 341-16 ([AISC 2016a](#)). In particular,
678 comparisons between the measured data and predictions from high-fidelity CFE column models
679 indicate that if GIs are neglected, then the predicted local buckling initiation as well as the
680 subsequent column damage progression is vastly different than that observed in reality. The
681 modeling recommendations by [Elkady and Lignos \(2018b\)](#) are deemed rational for simulating
682 cyclic plastic buckling of wide-flange steel columns.

683 The concept of a column repairability curve was also introduced. Based on the gathered
684 experimental data, these curves integrate in a single compact graphical format various column
685 performance indicators including the residual axial shortening, flange-tip in-plane deformation due
686 to local buckling and the column reserve capacity as a function of the story-drift demand. In
687 general, the column repairability curves presented herein indicate that when a column experiences
688 40mm flange-tip deformation ($\approx 7^\circ$ flange rotation angle) or 30mm residual axial shortening, its
689 reserve capacity is less than 80% of the attained peak flexural resistance. In that respect, the
690 interaction of a column with its concrete footing also affects the extent of column ([Inamasu et al.](#)

691 2017). This is outside the scope of the present study since the considered test specimens were
692 idealized with a fixed end boundary condition.

693 Finally, comparisons of the gathered experimental results with those from prior related studies
694 indicate that scale effects shall be carefully considered in order to properly trace the primary
695 column instability mode. The interaction between a wide-flange cross-section's flange and web
696 shall be considered to properly define section classification limits to control the axial shortening
697 and the cyclic deterioration in flexural strength of steel columns for seismic applications.

698 **Acknowledgements**

699 This study was based on work supported by the Natural Sciences and Engineering Research
700 Council of Canada (NSERC) under the Discovery Grant Program. The test specimen material and
701 fabrication was generously donated by ADF Corporation Inc. Additional support for the second
702 author was provided by the Swiss National Science Foundation (Award Number 200021_169248)
703 as well as École Polytechnique Fédérale de Lausanne (EPFL). The financial support is gratefully
704 acknowledged. The authors would like to sincerely thank Dr. William Cook, Mr. John Bartczak at
705 Jamieson Structural Laboratory at McGill University as well as Prof. Colin Rogers for their
706 invaluable assistance for the successful completion of the testing program. Any opinions, findings,
707 and conclusions or recommendations expressed in this paper are those of the authors and do not
708 necessarily reflect the views of sponsors.

709 **References**

- 710 ABAQUS-FEA/CAE. (2011). Dassault Systemes Simulia Corp., RI, USA. © Dassault Systèmes,
711 2010.
- 712 AISC (2016a). "Seismic provisions for structural steel buildings." *ANSI/AISC 341-16*, Chicago, IL
- 713 AISC (2016b). "Specification for structural steel buildings ".*ANSI/AISC 360-16*, Chicago, IL
- 714 Akcelyan, S., and Lignos, D. G. (2018). "Seismic retrofit of steel tall buildings with bilinear oil
715 dampers." *Proc., 16th European Conf. on Earthquake Eng.*, Thessaloniki, Greece.
- 716 Araújo, M., Macedo, L., and Castro, J. M. (2017). "Evaluation of the rotation capacity limits of
717 steel members defined in EC8-3." *J. of Constructional Steel Research*, 135, 11-29. DOI:
718 [10.1016/j.jcsr.2017.04.004](https://doi.org/10.1016/j.jcsr.2017.04.004).
- 719 Alavi, B., and Krawinkler, H. (2004). "Behavior of moment-resisting frame structures subjected
720 to near-fault ground motions." *Earthquake Eng. & Structural Dynamics*, 33(6), 687-706.
721 DOI: [10.1002/eqe.369](https://doi.org/10.1002/eqe.369).
- 722 Armstrong, P. J., and Frederick, C. O. (1966). "A mathematical representation of the multiaxial
723 bauschinger effect." *Materials at High Temperatures*, 24(1), 1-26. DOI:
724 [10.1179/096034007X207589](https://doi.org/10.1179/096034007X207589).

- 725 ASCE (1971). "Plastic design in steel, a guide and commentary." *Manual of Practice No. 41*, New
726 York, USA.
- 727 ASCE (2014). "Seismic evaluation and retrofit of existing buildings." *ASCE/SEI 41-13*, Reston,
728 VA.
- 729 ASTM (2014). "Standard specification for general requirements for rolled structural steel bars,
730 plates, shapes, and sheet piling." *ASTM A6/A6M-14*, ASTM International, West
731 Conshohocken, PA, USA.
- 732 ASTM (2015). "Standard specification for structural steel shapes." *ASTM A992/A992M*, ASTM
733 International, West Conshohocken, PA, USA.
- 734 AWS (2009). "Structural welding code - seismic supplement." *AWS D1.8/D1.8M:2009*, Miami, FL,
735 USA.
- 736 Bech, D., Tremayne, B., and Houston, J. (2015). "Proposed changes to steel column evaluation
737 criteria for existing buildings." *Proc., 2nd ATC-SEI Conf. on Improving the Seismic
738 Performance of Existing Building and Other Structures*, San Francisco, CA, USA.
- 739 Bruneau, M., Uang, C.-M., and Sabelli, S. R. (2011). *Ductile design of steel structures*, McGraw
740 Hill Professional.
- 741 Chen, Y., Cheng, X., and Nethercot, D. A. (2013). "An overview study on cross-section
742 classification of steel H-sections." *J. of Constructional Steel Research*, 80, 386-393. DOI:
743 [10.1016/j.jcsr.2012.10.006](https://doi.org/10.1016/j.jcsr.2012.10.006).
- 744 Cheng, X., Chen, Y., and Nethercot, D. A. (2013a). "Experimental study on H-shaped steel beam-
745 columns with large width-thickness ratios under cyclic bending about weak-axis." *Eng.
746 Structures*, 49, 264-274. DOI: [10.1016/j.engstruct.2012.10.035](https://doi.org/10.1016/j.engstruct.2012.10.035).
- 747 Cheng, X., Chen, Y., and Pan, L. (2013b). "Experimental study on steel beam–bolumns composed
748 of slender H-sections under cyclic bending." *J. of Constructional Steel Research*, 88, 279-
749 288. DOI: [10.1016/j.jcsr.2013.05.020](https://doi.org/10.1016/j.jcsr.2013.05.020).
- 750 Clark, P., Frank, K., Krawinkler, H., and Shaw, R. (1997). "Protocol for fabrication, inspection,
751 testing, and documentation of beam-column connection tests and other experimental
752 specimens". *Report no. SAC/BD-97*. SAC Joint Venture, Sacramento, CA.
- 753 Clifton, C., Bruneau, M., MacRae, G., Leon, R., and Fussell, A. (2011). "Steel structures damage
754 from the Christchurch earthquake series of 2010 and 2011." *Bulletin of the New Zealand
755 Society for Earthquake Eng.*, 44(4), 297-318.
- 756 Do, T. N., and Filippou, F. C. (2018). "A damage model for structures with degrading response."
757 *Earthquake Eng. & Structural Dynamics*, 47(2), 311-332. DOI: [10.1002/eqe.2952](https://doi.org/10.1002/eqe.2952).
- 758 Elkady, A., Ghimire, S., and Lignos, D. G. (2018). "Fragility curves for wide-flange steel columns
759 and implications on building-specific earthquake-induced loss assessment." *Earthquake
760 Spectra*. DOI: [10.1193/122017EQS260M](https://doi.org/10.1193/122017EQS260M).
- 761 Elkady, A., and Lignos, D. G. (2014). "Modeling of the composite action in fully restrained beam-
762 to-column connections: implications in the seismic design and collapse capacity of steel
763 special moment frames." *Earthquake Eng. & Structural Dynamics*, 43(13), 1935-1954.
764 DOI: [10.1002/eqe.2430](https://doi.org/10.1002/eqe.2430).
- 765 Elkady, A., and Lignos, D. G. (2015a). "Analytical investigation of the cyclic behavior and plastic
766 hinge formation in deep wide-flange steel beam-columns." *Bulletin Earthquake Eng*, 13(4),
767 1097-1118. DOI: [10.1007/s10518-014-9640-y](https://doi.org/10.1007/s10518-014-9640-y).
- 768 Elkady, A., and Lignos, D. G. (2015b). "Effect of gravity framing on the overstrength and collapse
769 capacity of steel frame buildings with perimeter special moment frames." *Earthquake Eng.
770 & Structural Dynamics*, 44(8), 1289–1307. DOI: [10.1002/eqe.2519](https://doi.org/10.1002/eqe.2519).

- 771 Elkady, A., and Lignos, D. G. (2016). "Dynamic stability of deep and slender wide-flange steel
772 columns-full scale experiments." *Proc. of the Annual Stability Conf., Orlando, Florida.*
773 Elkady, A., and Lignos, D. G. (2018a). "Full-scale testing of deep wide-flange steel columns under
774 multi-axis cyclic loading: Loading sequence, boundary effects and out-of-plane brace force
775 demands." *ASCE J. of Structural Eng.*, 144(2). DOI: [10.1061/\(ASCE\)ST.1943-
776 541X.0001937](https://doi.org/10.1061/(ASCE)ST.1943-541X.0001937).
- 777 Elkady, A., and Lignos, D. G. (2018b). "Improved seismic design and nonlinear modeling
778 recommendations for wide-flange steel columns." *ASCE J. of Structural Eng.*, 144(9).
779 DOI: [10.1061/\(ASCE\)ST.1943-541X.0002166](https://doi.org/10.1061/(ASCE)ST.1943-541X.0002166).
- 780 FEMA (2000). "State of the art report on connection performance." *Report FEMA-355D*, Federal
781 Emergency Management Agency, Washington, DC.
- 782 FEMA (2009a). "Fragility curves for components of steel SMF systems." *Background Document
783 FEMA P-58/BD-3.8.3*, Federal Emergency Management Agency, Washington, DC.
- 784 FEMA (2009b). "Quantification of building seismic performance factors." *Report FEMA-P695*,
785 Federal Emergency Management Agency, Washington, DC.
- 786 Fogarty, J., and El-Tawil, S. (2015). "Collapse resistance of steel columns under combined axial
787 and lateral loading." *J. of Structural Eng.*, 142(1). DOI: [10.1061/\(ASCE\)ST.1943-541X.0001350](https://doi.org/10.1061/(ASCE)ST.1943-
788 541X.0001350).
- 789 Gupta, A., and Krawinkler, H. (2000). "Behavior of ductile SMRFs at various seismic hazard
790 levels." *J. of Structural Eng.*, 126(1), 98-107. DOI: [10.1061/\(ASCE\)0733-9445\(2000\)126:1\(98\)](https://doi.org/10.1061/(ASCE)0733-
791 9445(2000)126:1(98)).
- 792 Hamburger, R., Deierlein, G. G., Lehman, D. E., Lignos, D. G., Lowes, L. N., Pekelnicky, R.,
793 Shing, P. B., Somers, P., and van de Lindt, J. W. (2018). "Recommended modeling
794 parameters and acceptance criteria for nonlinear analysis in support of seismic evaluation,
795 retrofit, and design." *NIST GCR 17-917-45*, Prepared for the U.S. Department of
796 Commerce and the National Institute of Standards and Technology (NIST) by the Applied
797 Technology Council (ATC).
- 798 Haselton, C. B., Liel, A. B., Lange, S. T., and Deierlein, G. G. (2008). "Beam-column element
799 model calibrated for predicting flexural response leading to global collapse of RC frame
800 buildings." *Report No. 2007/03*, Pacific Earthquake Eng. Research Center, Berkeley, CA,
801 USA.
- 802 Ibarra, L., and Krawinkler, H. (2005). "Global collapse of frame structures under seismic
803 excitations." *Report No. 152*, The John A. Blume Earthquake Eng. Center, Stanford
804 University, California, USA.
- 805 Ibarra, L. F., Medina, R. A., and Krawinkler, H. (2005). "Hysteretic models that incorporate
806 strength and stiffness deterioration." *Earthquake Eng. & Structural Dynamics*, 34(12),
807 1489-1511. DOI: [10.1002/eqe.495](https://doi.org/10.1002/eqe.495).
- 808 Inamasu, H., Lignos, D. G., and Kanvinde, A. (2017). "Effect of column base flexibility on the
809 hysteretic response of wide-flange steel columns." *Proc., 3rd Huixian Int. Forum on
810 Earthquake Eng. for Young Researchers*, Urbana-Champaign, Illinois, USA.
- 811 Kanno, R. (2016). "Advances in steel materials for innovative and elegant steel structures in Japan-
812 a review." *Structural Eng. Int.*, 26(3), 242-253. DOI:
813 [10.2749/101686616X14555428759361](https://doi.org/10.2749/101686616X14555428759361).
- 814 Kolwankar, S., Kanvinde, A., Kenawy, M., Lignos, D. G., and Kunnath, S. K. (2018). "Simulating
815 local buckling-induced softening in steel members using an equivalent nonlocal material

- model in displacement-based fiber elements." *J. of Structural Eng.*, 144(10), 04018192. DOI: [10.1061/\(ASCE\)ST.1943-541X.0002189](https://doi.org/10.1061/(ASCE)ST.1943-541X.0002189).
- Krawinkler, H. (2009). "Loading histories for cyclic tests in support of performance assessment of structural components." *Proc., 3rd Int. Conf. on Advances in Experimental Structural Eng.*, San Francisco, CA, USA, 15-16.
- Krawinkler, H., Zohrei, M., Lashkari-Irvani, B., Cofie, N. G., and Hadidi-Tamjed, H. (1983). "Recommendations for experimental studies on the seismic behavior of steel components and materials." *Report No. 61*, The John A. Blume Earthquake Eng. Center, Stanford University, California, USA.
- LATBSDC (2017). "An alternative procedure for the analysis and design of tall buildings located in the los angeles region." Los Angeles, CA, USA.
- Lemaitre, J., and Chaboche, J. (1975). "A non-linear model of creep-fatigue damage cumulation and interaction (for hot metallic structures)." *Mechanics of visco-elastic media and bodies*.
- Lignos, D., Krawinkler, H., and Whittaker, A. (2011a). "Prediction and validation of sidesway collapse of two scale models of a 4-story steel moment frame." *Earthquake Eng. & Structural Dynamics*, 40(7), 807-825, DOI: [10.1002/eqe.1061](https://doi.org/10.1002/eqe.1061).
- Lignos, D. G., Chung, Y., Nagae, T., and Nakashima, M. (2011b). "Numerical and experimental evaluation of seismic capacity of high-rise steel buildings subjected to long duration earthquakes." *Computers & Structures*, 89(11), 959-967, DOI: [10.1016/j.compstruc.2011.01.017](https://doi.org/10.1016/j.compstruc.2011.01.017).
- Lignos, D. G., Hartloper, A., Elkady, A., Hamburger, R., and Deierlein, G. G. (2018). "Proposed updates to the ASCE 41 nonlinear modeling parameters for wide-flange steel columns in support of performance-based seismic engineering." *J. of Structural Eng.* (under review).
- Lignos, D. G., Hikino, T., Matsuoka, Y., and Nakashima, M. (2013). "Collapse assessment of steel moment frames based on E-Defense full-scale shake table collapse tests." *J. of Structural Eng.*, 139(1), 120-132. DOI: [10.1061/\(ASCE\)ST.1943-541X.0000608](https://doi.org/10.1061/(ASCE)ST.1943-541X.0000608).
- Lignos, D. G., and Krawinkler, H. (2011). "Deterioration modeling of steel components in support of collapse prediction of steel moment frames under earthquake loading." *J. of Structural Eng.*, 137(11), 1291-1302. DOI: [10.1061/\(ASCE\)ST.1943-541X.0000376](https://doi.org/10.1061/(ASCE)ST.1943-541X.0000376).
- Lignos, D. G., and Krawinkler, H. (2013). "Development and utilization of structural component databases for performance-based earthquake engineering." *J. of Structural Eng.*, 139(8), 1382-1394. DOI: [10.1061/\(ASCE\)ST.1943-541X.0000646](https://doi.org/10.1061/(ASCE)ST.1943-541X.0000646).
- MacRae, G. A., Carr, A. J., and Walpole, W. R. (1990). "The seismic response of steel frames." *Report No. 90-6*, Department of Civil Eng., University of Canterbury, New Zealand.
- MacRae, G. A., Urmonson, C. R., Walpole, W. R., Moss, P., Hyde, K., and Clifton, C. (2009). "Axial shortening of steel columns in buildings subjected to earthquakes." *Bulletin of the New Zealand Society for Earthquake Eng.*, 42(4), 275.
- Maison, B. F., and Speicher, M. S. (2016). "Loading Protocols for ASCE 41 Backbone Curves." *Earthquake Spectra*, 32(4), 2513-2532. DOI: [10.1193/010816EQS007EP](https://doi.org/10.1193/010816EQS007EP).
- Miyamura, T., Yamashita, T., Akiba, H., and Ohsaki, M. (2015). "Dynamic FE simulation of four-story steel frame modeled by solid elements and its validation using results of full-scale shake-table test." *Earthquake Eng. & Structural Dynamics*, 44(9), 1449-1469. DOI: [10.1002/eqe.2526](https://doi.org/10.1002/eqe.2526).
- Nakashima, M., Nagae, T., Enokida, R., and Kajiwara, K. (2018). "Experiences, accomplishments, lessons, and challenges of E-Defense tests using world's largest shaking table." *Japan Architectural Review*, 1(1), 4-17. DOI: [10.1002/2475-8876.10020](https://doi.org/10.1002/2475-8876.10020).

- 862 Nakashima, M., Takanashi, K., and Kato, H. (1990). "Test of steel beam-columns subject to
863 sidesway." *J. of Structural Eng.*, 116(9), 2516-2531. DOI: [10.1061/\(ASCE\)0733-9445\(1990\)116:9\(2516\)](https://doi.org/10.1061/(ASCE)0733-9445(1990)116:9(2516)).
- 864
- 865 Newell, J. D., and Uang, C.-M. (2006). "Cyclic behavior of steel columns with combined high
866 axial load and drift demand." *Report No. SSRP-06/22*, Department of Structural Eng.,
867 University of California, San Diego.
- 868 NIST (2010a). "Evaluation of the FEMA P695 methodology for quantification of building seismic
869 performance factors." *NIST GCR 10-917-8*, NEHRP consultants Joint Venture.
- 870 NIST (2010b). "Research plan for the study of seismic behaviour and design of deep slender wide
871 flange structural steel beam-column members." *NIST GCR 11-917-13*, NEHRP consultants
872 Joint Venture.
- 873 Okazaki, T., Lignos, D. G., Midorikawa, M., Ricles, J. M., and Love, J. (2013). "Damage to steel
874 buildings observed after the 2011 Tohoku-Oki earthquake." *Earthquake Spectra*, 29(S1),
875 S219-S243. DOI: [10.1193/1.4000124](https://doi.org/10.1193/1.4000124).
- 876 Ozkula, G., Harris, J., and Uang, C. M. (2017). "Observations from cyclic tests on deep, wide-
877 flange beam-columns." *AISC Eng. J.*, 54(1), 45-61.
- 878 PEER (2017). "Guidelines for performance-based seismic design of tall buildings." *Report No.*
879 *2017/06*, Pacific Earthquake Eng. Center, Berkeley, California, USA.
- 880 PEER/ATC (2010). "Modeling and acceptance criteria for seismic design and analysis of tall
881 buildings." *PEER/ATC 72-1*, Redwood City, CA.
- 882 Peng, B. H., MacRae, G. A., Walpole, W. R., Moss, P., Dhakal, R., and Clifton, C. (2008). "Plastic
883 hinge location in columns of steel frames subjected to seismic actions." *Bulletin of the New*
884 *Zealand Society for Earthquake Eng.*, 41(1).
- 885 Pericoli, V., and Kanvinde, A. (2018). "Theoretical study of ductile fracture in steel structures in
886 the presence of spatial variability in toughness." *J. of Structural Eng.*, 144(5), 04018024,
887 DOI: [10.1061/\(ASCE\)ST.1943-541X.0002008](https://doi.org/10.1061/(ASCE)ST.1943-541X.0002008).
- 888 Popov, E. P., Bertero, V. V., and Chandramouli, S. (1975). "Hysteretic behavior of steel columns."
889 *Report No. EERC 75-11*, Earthquake Engineering Research Center, Berkeley, CA, USA.
- 890 Shirasawa, H., Kobayashi, H., and Jizaimaru, J. (1981). "The effect of various strengthening
891 methods on ductility of high strength steel sheets." *Tetsu-to-Hagane (J. of the Iron and*
892 *Steel Institute of Japan)*, 67(14), 2208-2215.
- 893 SNZ (2007). "Steel structures standard." *NZS 3404:2007*, Wellington, New Zealand.
- 894 Sousa, A. A., and Lignos, D. G. (2018). "On the inverse problem of classic nonlinear plasticity
895 models." *EPFL-REPORT-231968*, Ecole Polytechnique Federale de Lausanne (EPFL),
896 Lausanne, Switzerland.
- 897 Stoakes, C. D., and Fahnstock, L. A. (2016). "Strong-axis stability of wide flange steel columns
898 in the presence of weak-axis flexure." *J. of Structural Eng.*, 142(5), DOI:
899 [10.1061/\(ASCE\)ST.1943-541X.0001448](https://doi.org/10.1061/(ASCE)ST.1943-541X.0001448).
- 900 Suzuki, Y., and Lignos, D. G. (2014). "Development of loading protocols for experimental testing
901 of steel columns subjected to combined high axial load and lateral drift demands near
902 collapse." *Proc. of the 10th National Conf. on Earthquake Eng.*, Anchorage, Alaska, USA.
- 903 Suzuki, Y., and Lignos, D. G. (2015a). "Large scale collapse experiments of wide-flange steel
904 beam-columns." *Proc. of the 8th Int. Conf. on Behavior of Steel Structures in Seismic Areas*,
905 Shanghai, China.

- 906 Suzuki, Y., and Lignos, D. G. (2017). "Collapse behavior of steel columns as part of steel frame
907 buildings: Experiments and numerical models." *Proc., 16th World Conf. on Earthquake
908 Eng.*, Santiago, Chile.
- 909 Tirca, L., Chen, L., and Tremblay, R. (2015). "Assessing collapse safety of cbf buildings subjected
910 to crustal and subduction earthquakes." *J. of Constructional Steel Research*, 115, 47-61.
911 DOI: [10.1016/j.jcsr.2015.07.025](https://doi.org/10.1016/j.jcsr.2015.07.025).
- 912 Toutant, G., Minouei, Y. B., Imanpour, A., Koboevic, S., and Tremblay, R. (2017). "Stability of
913 steel columns in steel concentrically braced frames subjected to seismic loading." *Proc.,
914 ASCE Structures Congress*, Denver, Colorado, USA.
- 915 Uang, C.-M., and Bruneau, M. (2018). "State-of-the-art review on seismic design of steel
916 structures." *J. of Structural Eng.*, 144(4), 03118002. DOI: [10.1061/\(ASCE\)ST.1943-541X.0001973](https://doi.org/10.1061/(ASCE)ST.1943-541X.0001973).
- 918 Voce, E. (1948). "The relationship between stress and strain for homogeneous deformation." *J.
919 of the Institute of Metals*, 74, 537-562.
- 920 Wu, T.-U., El-Tawil, S., and McCormick, J. (2018a). "Seismic collapse response of steel moment
921 frames with deep columns." *J. of Structural Eng.*, 144(9), 04018145. DOI:
922 [10.1061/\(ASCE\)ST.1943-541X.0002150](https://doi.org/10.1061/(ASCE)ST.1943-541X.0002150).
- 923 Wu, T.-Y., El-Tawil, S., and McCormick, J. (2018b). "Highly ductile limits for deep steel
924 columns." *J. of Structural Eng.*, 144(4), 04018016. DOI: [10.1061/\(ASCE\)ST.1943-541X.0002002](https://doi.org/10.1061/(ASCE)ST.1943-541X.0002002).
- 926 Zargar, S., Medina, R. A., and Miranda, E. (2014). "Cyclic behavior of deep steel columns
927 subjected to large drifts, rotations, and axial loads." *Proc., 10th National Conf. on
928 Earthquake Eng.*, Anchorage, AK, USA.
- 929 Zeimian, R. D., Abreu, J. C. B., Denavit, M. D., and Denavit, T.-J. L. (2018). "Three-Dimensional
930 Benchmark Problems for Design by Advanced Analysis: Impact of Twist." *J. of Structural
931 Eng.* 144(12), 04018220. DOI: [10.1061/\(ASCE\)ST.1943-541X.0002224](https://doi.org/10.1061/(ASCE)ST.1943-541X.0002224).
- 932

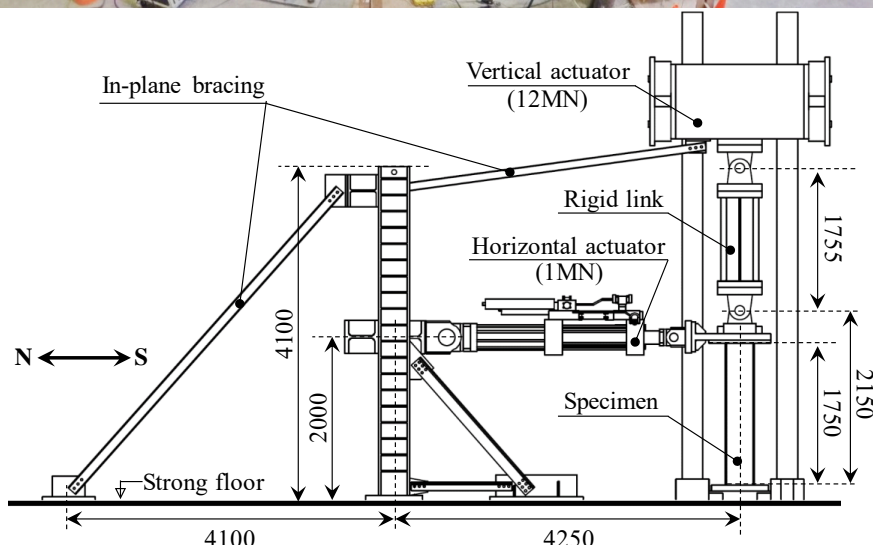
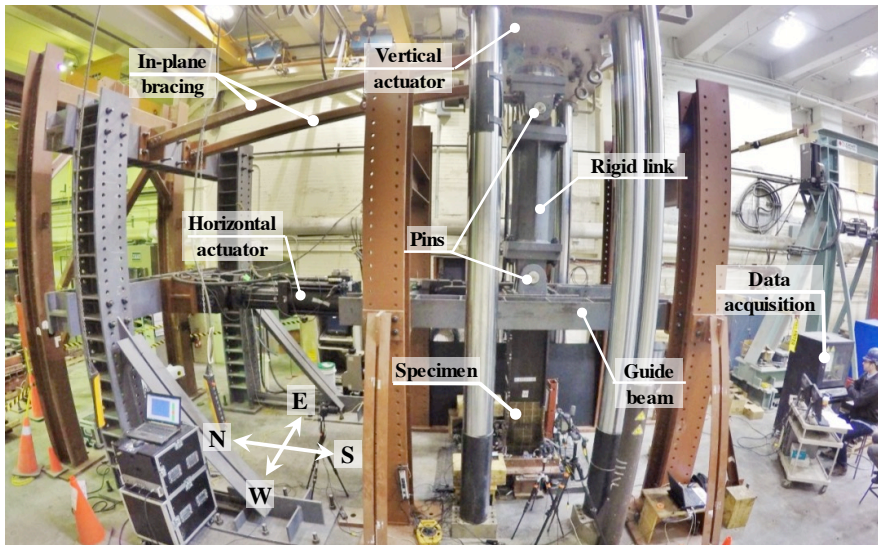
Table 1. Test matrix summary and measured geometric and material properties.

Spec. ID	Cross- Section	Lateral protocol	$\frac{P}{P_y}$	$\frac{b_f}{2t_f}$	$\frac{h}{t_w}$	$\frac{L_b}{r_y}$	Measured material properties [MPa]						
							E	$f_{y,mill}$	$f_{u,mill}$	$f_{y,w}$	$f_{y,f}$	$f_{u,w}$	$f_{u,f}$
A1	W14x61	Monotonic	30%										
A2	W14x61	Monotonic	50%				7.8	30.4	29.3	202315	384	493	374
A3	W14x61	Collapse-consistent	50%										358
A4	W14x61	Symmetric	30%±45%										471
B1	W16x89	Monotonic	30%										
B2	W16x89	Monotonic	50%				5.9	25.9	28.9	199402	379	514	383
B3	W16x89	Symmetric	50%										368
B4	W16x89	Symmetric	50%±25%										491
C1	W14x82	Monotonic	30%										
C2	W14x82	Monotonic	50%				5.9	22.4	29.0	199873	379	539	411
C3	W14x82	Symmetric	50%										383
C4	W14x82	Symmetric	75%										531
													537

h : web height; t_w : web thickness; b_f : flange width; t_f : flange thickness; L_b : laterally unbraced length; r_y : weak-axis' radius of gyration;

E : elastic modulus; $f_{y,mill}$ and $f_{u,mill}$: yield and ultimate stress, respectively, based on mill certificate; $f_{y,w}$: web yield stress; $f_{y,f}$: flange yield stress; $f_{u,w}$: web ultimate stress; $f_{u,f}$: flange ultimate stress

936	List of Figures	
937		
938	Fig. 1. Overview of the test setup for experimental testing of cantilever steel column specimens [Dimensions in mm].....	62
939		
940	Fig. 2. Typical column specimen detail (Group A) [Dimensions in mm].....	63
941	Fig. 3. Employed loading protocols for experimental testing of steel columns.	64
942	Fig. 4. Illustration of deduced out-of-plane column deformation and in-plane flange deformation based on LED measurements.	65
943		
944	Fig. 5. End moment versus chord-rotation relation of tested specimens.....	66
945	Fig. 6. Column axial shortening versus chord-rotation relation of tested specimens.....	67
946	Fig. 7. Out-of-plane and flange tip displacements versus chord-rotation of selected specimens.	68
947	Fig. 8. Typical damage progression and geometric instability modes [*LB: Local buckling].....	69
948	Fig. 9. Evaluation of ANSI/AISC 360-16 axial force-bending (P-M) interaction curve.	70
949	Fig. 10. Variable axial load demands and corresponding column axial stiffness deterioration..	71
950	Fig. 11. Assessment of column plastic hinge length.	72
951	Fig. 12. Comparison of column specimens with different cross-section depths and end boundary conditions.	73
952		
953	Fig. 13. Typical column repairability curves.....	74
954	Fig. 14. Assessment of PEER/ATC 72-1 modeling guidelines for monotonic and first-cycle envelope curves of wide-flange steel columns.....	75
955		
956	Fig. 15. Ratio of theoretical-to-measured rotational stiffness for several past experimental programs.....	76
957		
958	Fig. 16. Assessment of predicted (a) pre- and (b) post-capping plastic rotations of wide-flange steel columns based on PEER/ATC 72-1 modeling recommendations.	77
959		
960	Fig. 17. Comparisons between CFE predictions and measured steel column hysteretic response.	78
961		
962		

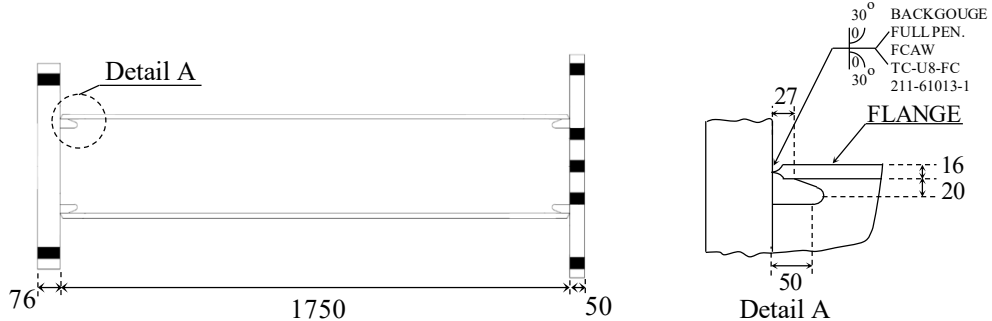


963

Fig. 1. Overview of the test setup for experimental testing of cantilever steel column specimens [Dimensions in mm].

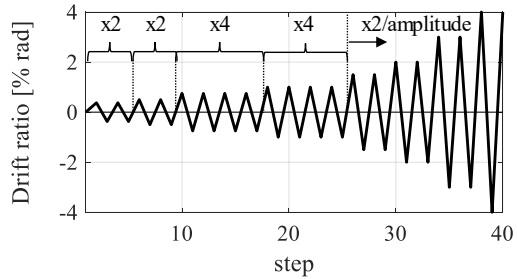
964

specimens [Dimensions in mm].

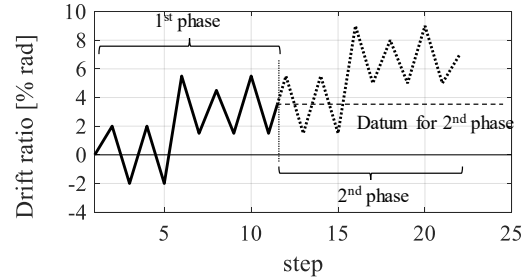


965

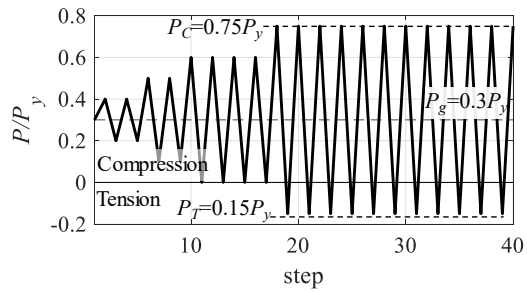
Fig. 2. Typical column specimen detail (Group A) [Dimensions in mm].



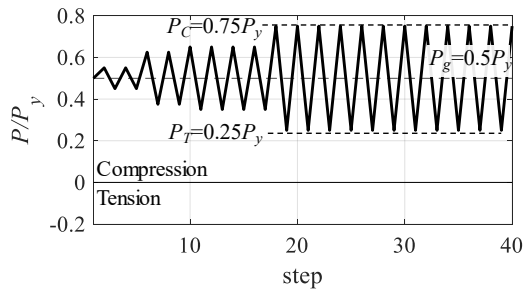
(a) Symmetric cyclic lateral loading protocol



(b) Collapse-consistent lateral loading protocol

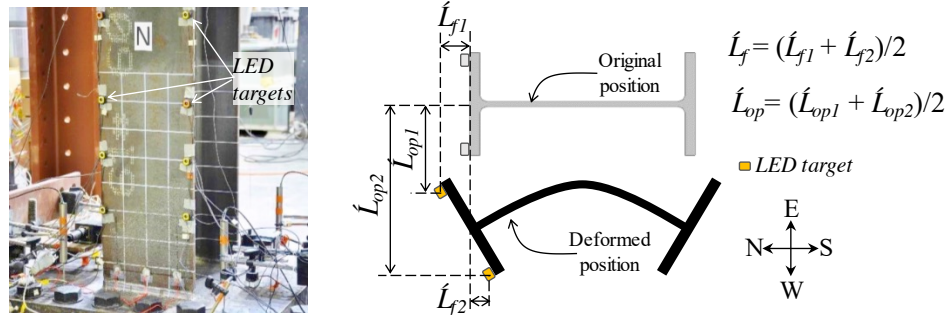


(c) Varying axial loading protocol
 $P_g/P_y=30\%\pm P_v/P_y=45\%$



(d) Varying axial loading protocol
 $P_g/P_y=50\%\pm P_v/P_y=25\%$

Fig. 3. Employed loading protocols for experimental testing of steel columns.



967

Fig. 4. Illustration of deduced out-of-plane column deformation and in-plane flange

968

deformation based on LED measurements.

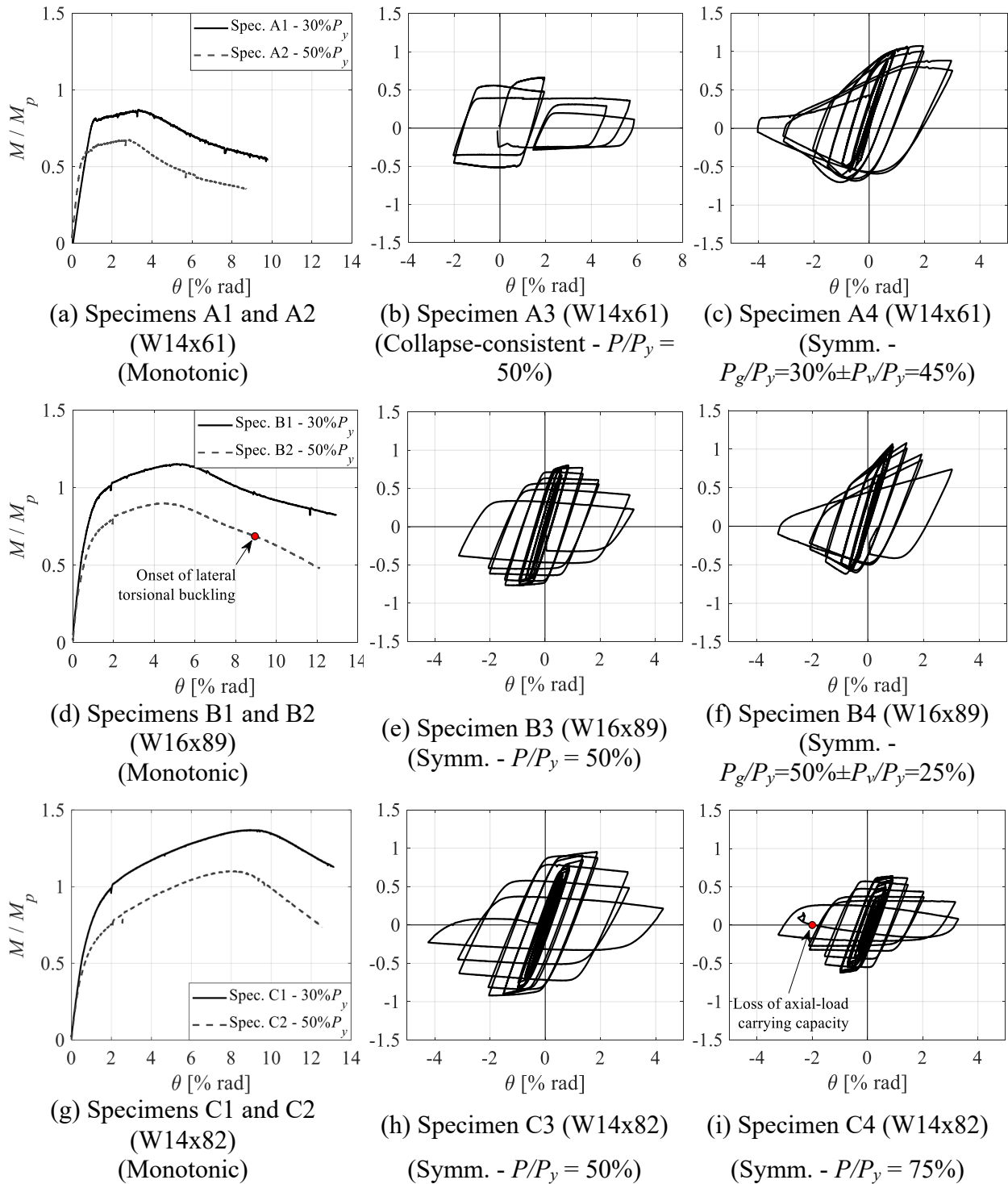
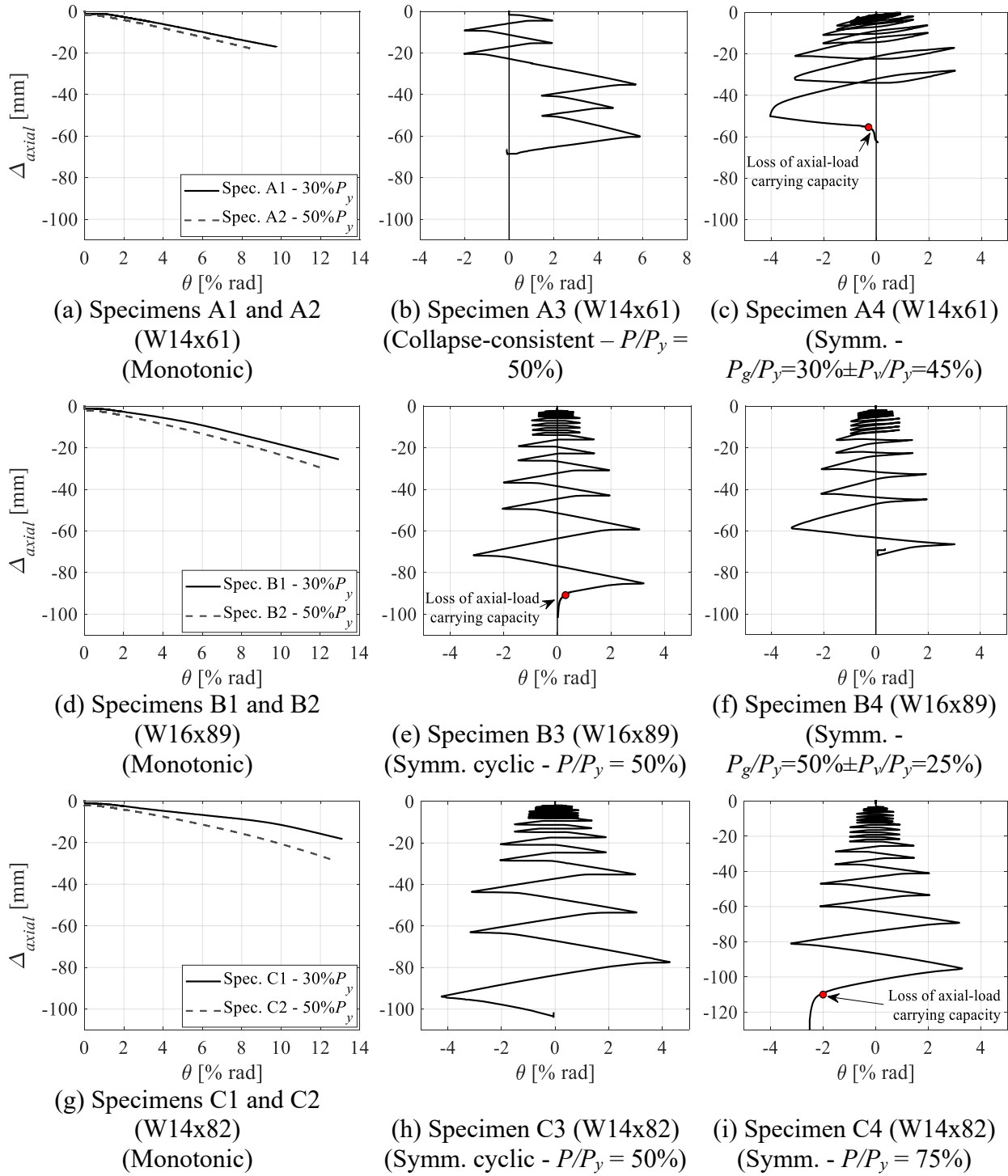


Fig. 5. End moment versus chord-rotation relation of tested specimens.

**Fig. 6.** Column axial shortening versus chord-rotation relation of tested specimens.

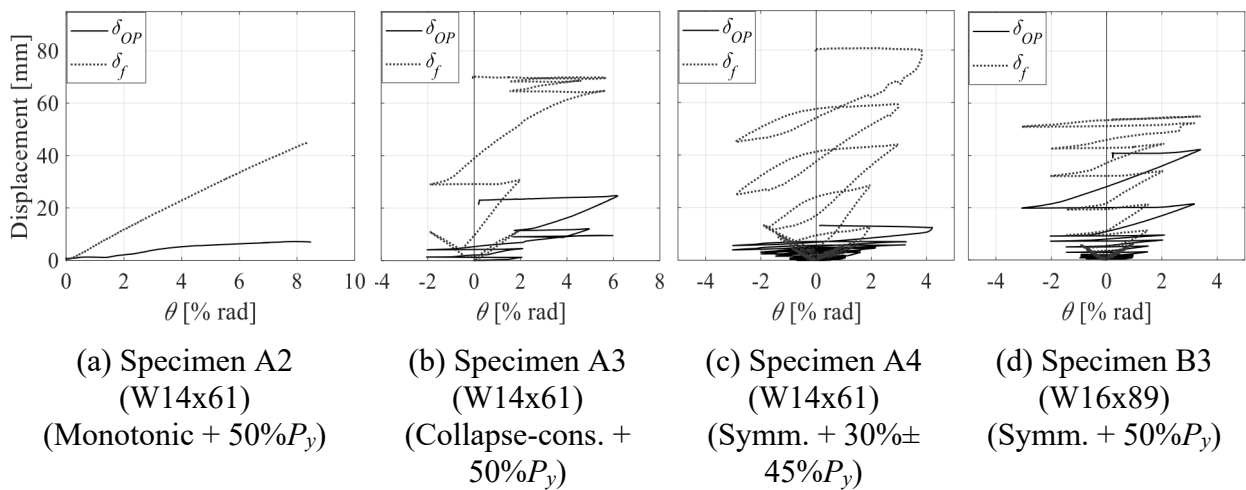
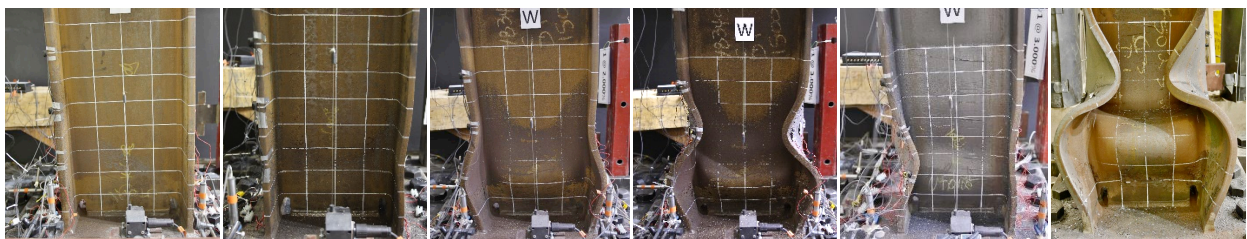
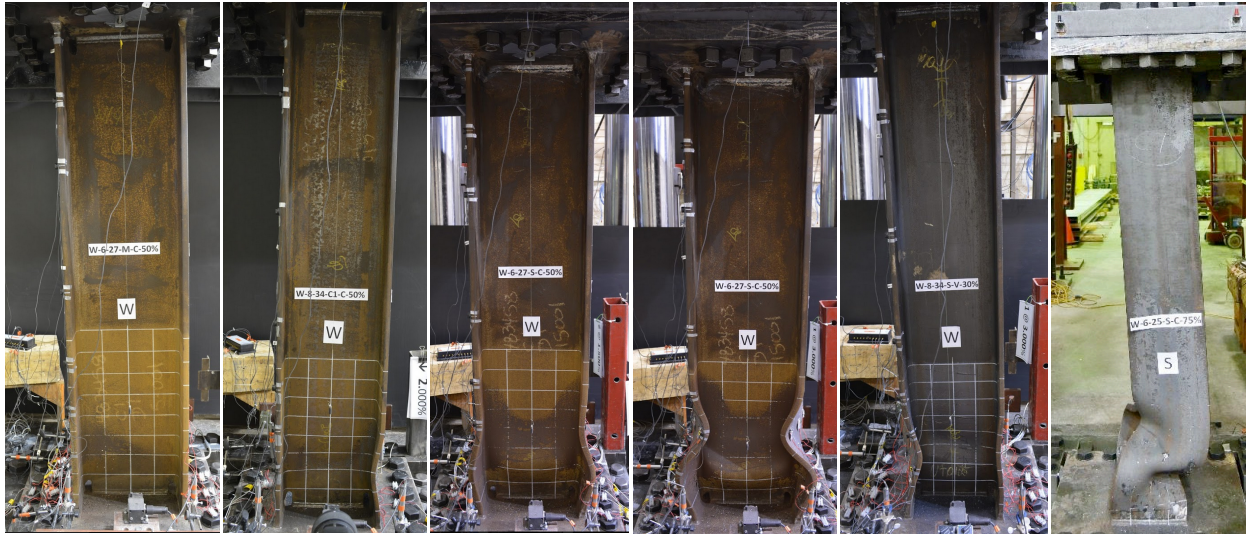


Fig. 7. Out-of-plane and flange tip displacements versus chord-rotation of selected specimens.



(a) Yeilding
(Monotonic +
50% P_y) (b) LB*
(Collapse
cons.+50% P_y) (c) Symm. LB*
(Symm.+50%
 P_y) (d) Double
wave LB*
(Symm.+50% P
 y) (e) Asymm.
LB*
(Symm.+30%
±45% P_y) (f) Loss of
axial load-
carrying
capacity
(Symm.+75%
 P_y)

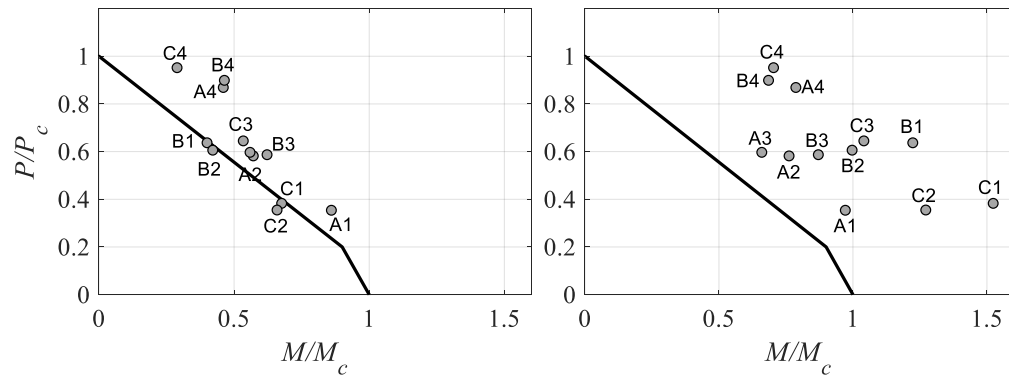
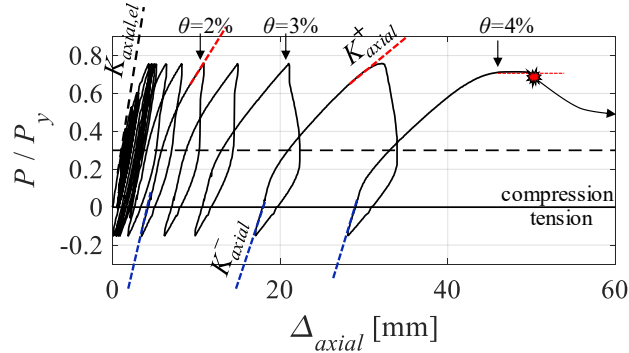
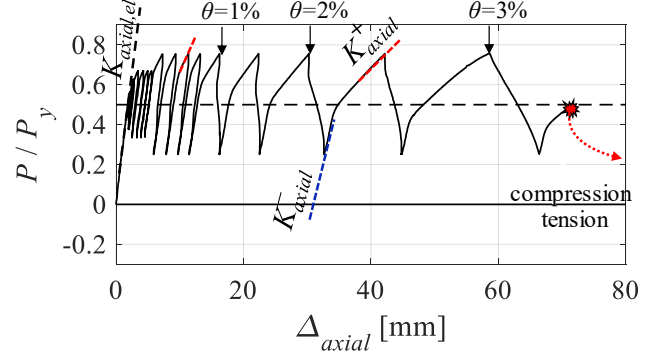


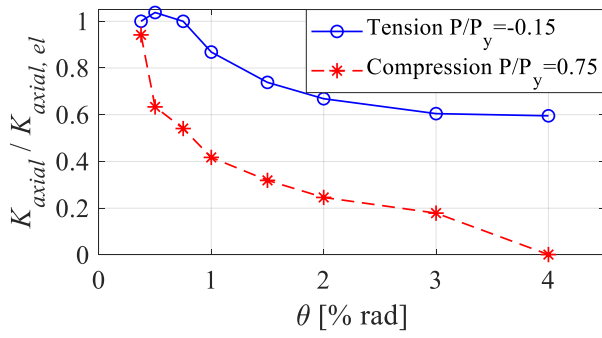
Fig. 9. Evaluation of ANSI/AISC 360-16 axial force-bending (P-M) interaction curve.



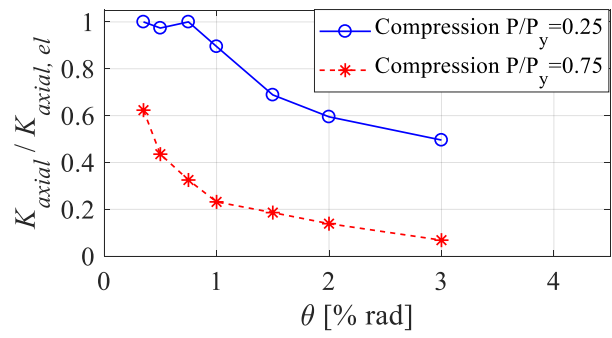
(a) Specimen A4



(b) Specimen B4

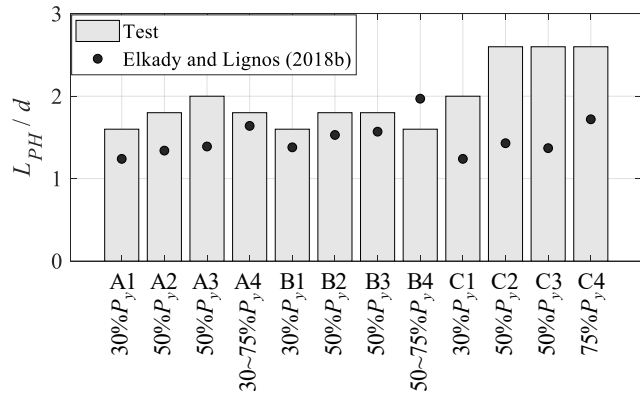


(c) Specimen A4

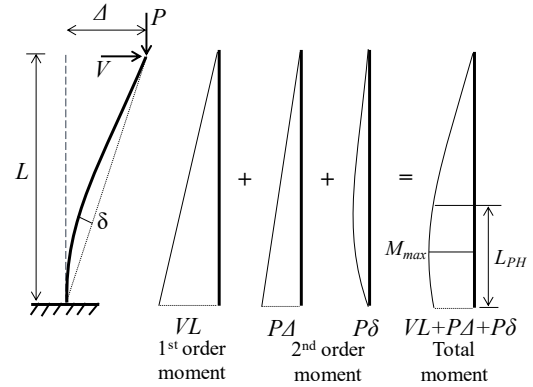


(d) Specimen B4

Fig. 10. Variable axial load demands and corresponding column axial stiffness deterioration.



(a) Measured and predicted plastic hinge length

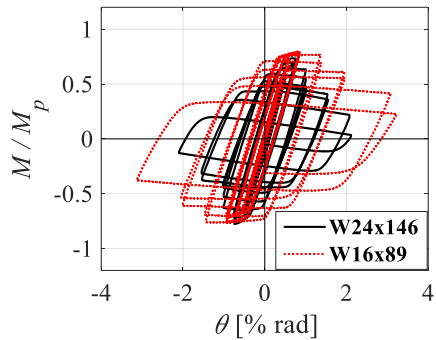


(b) second-order effects on plastic hinge length

Fig. 11. Assessment of column plastic hinge length.



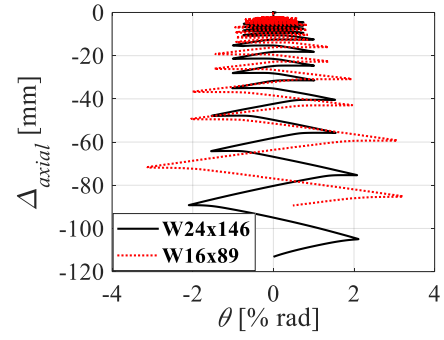
(a) Deformation profile at 2% drift
W16x89 (1.8m cantilever)



(c) Moment-rotation behavior at column base



(b) Deformation profile at 2% drift
W24x146 (4m fixed-end)



(d) Axial shorteing-rotation behavior

976

Fig. 12. Comparison of column specimens with different cross-section depths and end

977

boundary conditions.

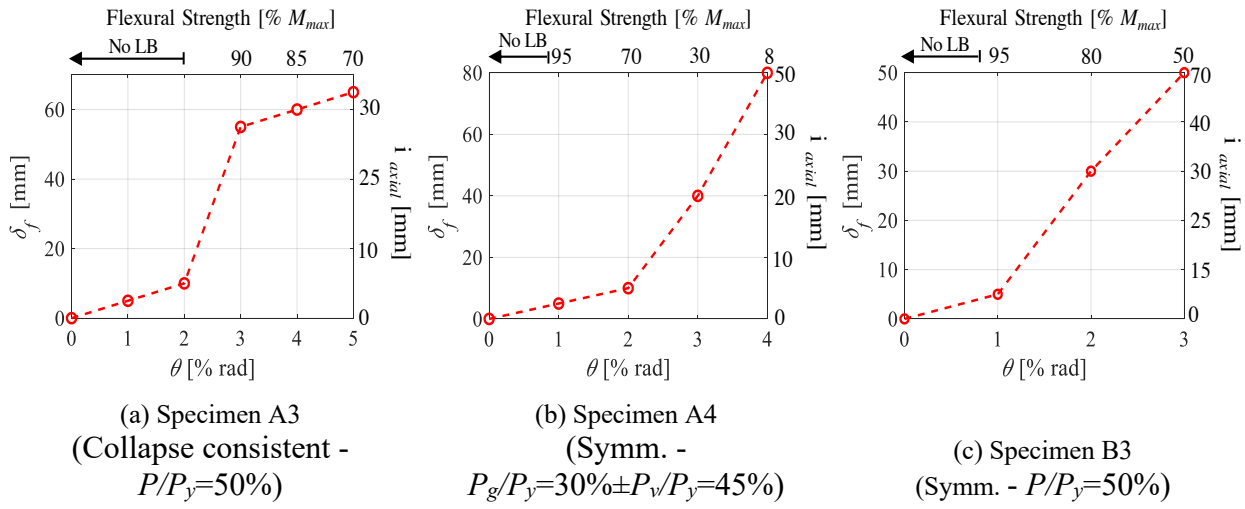
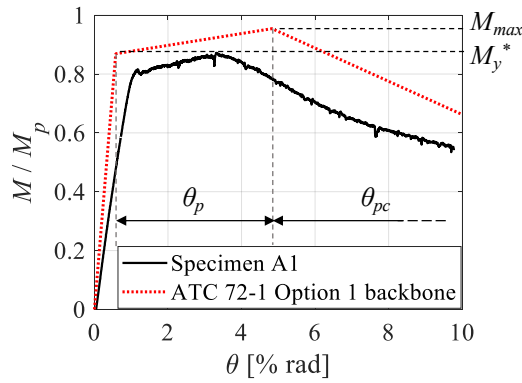
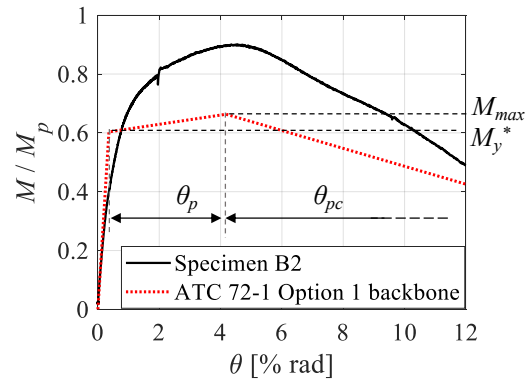


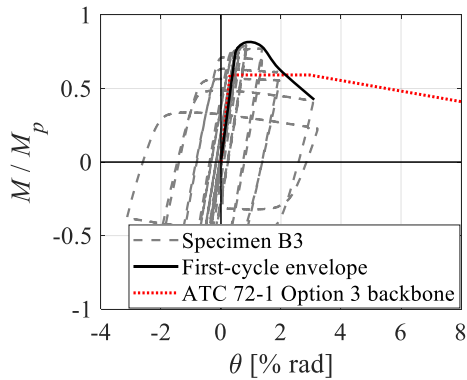
Fig. 13. Typical column repairability curves.



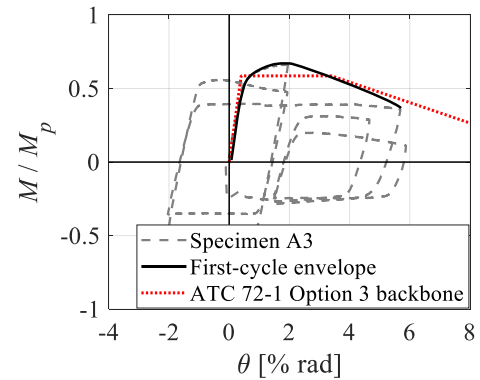
(a) Specimen A1



(b) Specimen B2



(c) Specimen B3



(d) Specimen A3

979

Fig. 14. Assessment of PEER/ATC 72-1 modeling guidelines for monotonic and first-cycle

980

envelope curves of wide-flange steel columns.

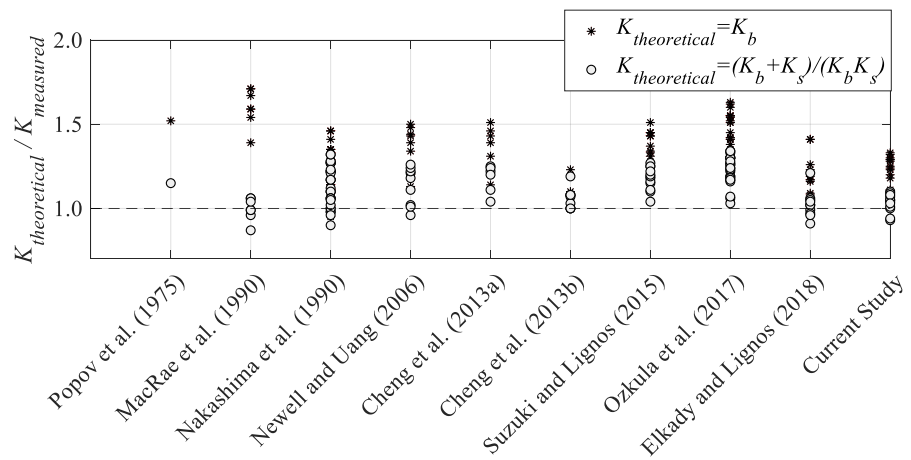


Fig. 15. Ratio of theoretical-to-measured rotational stiffness for several past experimental

programs.

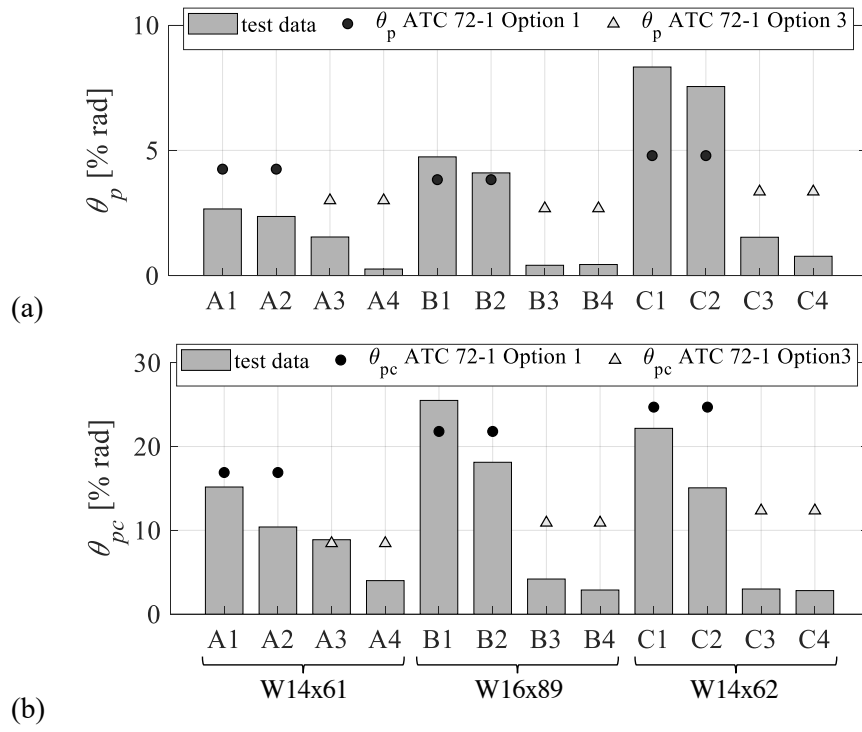


Fig. 16. Assessment of predicted (a) pre- and (b) post-capping plastic rotations of wide-flange steel columns based on PEER/ATC 72-1 modeling recommendations.

984

985

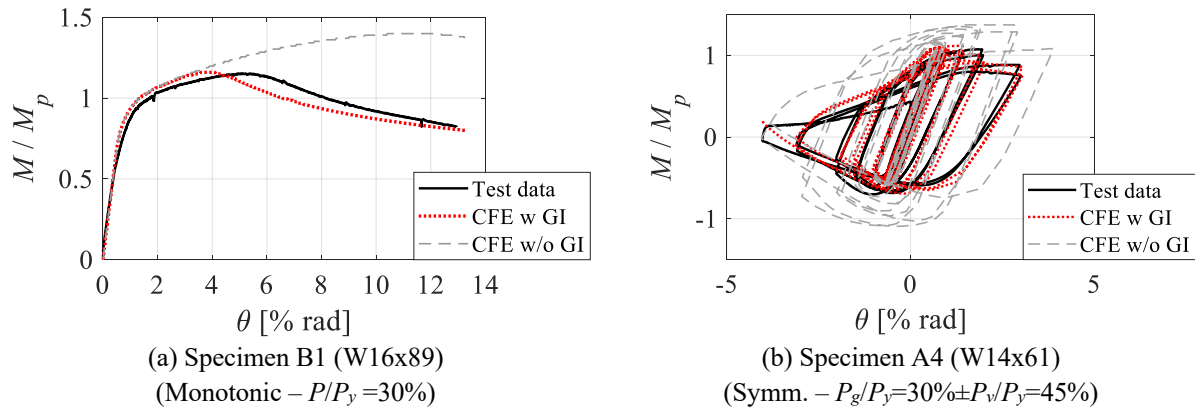


Fig. 17. Comparisons between CFE predictions and measured steel column hysteretic

986

response.

987

988